J. Mech. Phys. Solids 211 (2026) 106548

Contents lists available at ScienceDirect

Journal of the Mechanics and Physics of Solids

journal homepage: www.elsevier.com/locate/jmps

Dynamic Willis-framework homogenization for metabeams with active scatterers

Shaoyun Wang [a], Honghua Qian [a], Jiaji Chen [a], Nan Shao [a], Wen Cheng [b], Heng Jiang [c], Rui Zhu [d,*], Guoliang Huang [b,e,*]

[a] Department of Mechanical and Aerospace Engineering, University of Missouri, 65211, Columbia, MO, USA
[b] Department of Mechanics and Engineering Science, Peking University, 100871, Beijing, China
[c] Institute of Mechanics, Key Laboratory of Microgravity, Chinese Academy of Sciences, 100190, Beijing, China
[d] School of Aerospace Engineering, Beijing Institute of Technology, 100081, Beijing, China
[e] Faculty of Mechanical Engineering and Mechanics, Ningbo University, 315211, Ningbo, PR China

ARTICLE INFO

Keywords:
Active willis medium
Dynamic homogenization
Non-hermiticity
Nonlocality
Nonreciprocity
Topology

ABSTRACT

Active Willis media with asymmetric coupling offer a powerful platform for realizing nonreciprocal and non-Hermitian wave phenomena. However, existing homogenization theories are predominantly formulated for passive systems and are inadequate for capturing the complex dynamics of active media. In this work, we present a dynamic Willis homogenization framework tailored for elastic metabeams embedded with periodically distributed active scatterers. These scatterers are implemented using piezoelectric sensor-actuator pairs connected through programmable feedforward control, enabling tunable, direction-dependent interactions. By leveraging a source-driven homogenization approach, we derive a nonlocal, non-Hermitian effective Willis model that rigorously incorporates both frequency and spatial dispersion across the entire Brillouin zone. The model is validated through full-scale numerical simulations, demonstrating accurate reproduction of both the real and imaginary components of dispersion relations under various control configurations. The framework captures a range of hallmark non-Hermitian behaviors, including low-frequency shear-enhanced flexural modes, strong nonreciprocity, and skin modes arising under open boundary conditions. This study could provide a solid foundation for the design and dynamic control of non-Hermitian active metamaterials

1. Introduction

Willis media are generalized elastic continua characterized by couplings between momentum and strain, as well as stress and velocity-extending beyond the framework of classical elasticity theory (Willis, 1981, 1997). These couplings, which arise from symmetry breaking at the microscale, motivate the development of various homogenization approaches. Among them are Green's function and field averaging techniques (Willis, 2009, 2011, 2012; Milton and Willis, 2010; Nemat-Nasser and Srivastava, 2011; Shuvalov et al., 2011; Norris et al., 2012; Srivastava, 2015; Nassar et al., 2015), source-driven homogenization (Sieck et al., 2017; Li et al., 2024), asymptotic expansions (Nassar et al., 2016), perturbative methods (Qu et al., 2022; Milton, 2007), and modal subspace projections (Ponge et al., 2017; Pernas-Salomón and Shmuel, 2018). These frameworks extend to applications in acoustics (Muhlestein et al., 2017; Li et al., 2022, 2024) and piezoelectric media (Pernas-Salomón and Shmuel, 2020b; Pernas-Salomón et al., 2021; Pernas-Salomón

* Corresponding authors.
E-mail addresses: glhuang911@gmail.com, ruizhu@bit.edu.cn (R. Zhu), guohuang@pku.edu.cn (G. Huang).

https://doi.org/10.1016/j.jmps.2026.106548
Received 2 August 2025; Received in revised form 3 February 2026; Accepted 6 February 2026
Available online 14 February 2026

and Shmuel, 2020a; Lee et al., 2023; Baz, 2024; Muhafra et al., 2023), enabling advanced wave control strategies including cloaking (Milton et al., 2006; Chen and Haberman, 2023), asymmetric reflection (Liu et al., 2019; Muhlestein et al., 2017), polarization conversion (Qu et al., 2022), and independent tuning of reflection and transmission (Chen et al., 2020). In passive systems, strong Willis coupling is typically achieved through local resonances, which are inherently narrowband and limited in tunability. By contrast, active systems introduce programmable and broadband control via artificially active scatterers. Unlike passive counterparts, active systems generate non-Hermitian behavior by introducing controlled gain and/or loss mechanisms that break the energy-conserving nature of conventional dynamics. This is typically achieved by integrating external energy sources, such as feedback control loops or amplification circuits, into the physical structure of the system. For example, elastic metabeams integrated with piezoelectric circuits provide a tractable and highly tunable platform for realizing various non-Hermitian wave effects, including skin modes (Chen et al., 2021), odd mass density (Wu et al., 2023), temporal reflections (Wang et al., 2025), rainbow trapping (Chen et al., 2022), nonlinearity induced topological waves (Qian et al., 2025), and topological pumping (Xia et al., 2021). In particular, (Chen et al., 2020) realize nonreciprocal coupling in a piezoelectric beam through asymmetric feedforward control, effectively creating a non-Hermitia Willis metasurface. Recent efforts in active acoustic Willis media demonstrate gain and directionality using parameter retrieval methods (Cheng and Hu, 2022; Zhai et al., 2019), yet a comprehensive homogenization theory that incorporates dynamic and active microstructure effects remains largely unexplored. Among existing methods, only source-driven homogenization-originally formulated for passive materials-can systematically incorporate active and asymmetric scatterers, thereby providing a pathway to developing effective Willis constitutive relations (Sieck et al., 2017; Chen et al., 2020; Li et al., 2024).

On the other hand, non-Hermitian systems exhibit unique wave phenomena absent in traditional Hermitian physics. One such phenomenon is the non-Hermitian skin effect (NHSE), wherein bulk eigenmodes become exponentially localized near a boundary (Yao and Wang, 2018). The presence of NHSE challenges the validity of conventional Bloch band theory, prompting the development of non-Bloch band theory, which extends the wavenumber into the complex plane. Within this framework, the generalized Brillouin zone (GBZ) replaces the standard Brillouin zone, serving as a key analytical tool to determine the onset, strength, and direction of mode localization in non-Hermitian systems. While non-Bloch band theory provides a rigorous foundation for analyzing mode localization in non-Hermitian systems, most recent studies on non-Hermitian acoustic and elastic metamaterials (Chen et al., 2021; Wang et al., 2024; Wu et al., 2024) focus on the observation and characterization of skin modes and winding numbers without incorporating GBZ-based analysis. Moreover, these studies typically rely on local constitutive models, which neglect frequency (temporal) and wavenumber (spatial) dispersion. This omission leads to incomplete dispersion spectra-particularly at high frequencies or short wavelengths-limiting the accurate computation of winding numbers and the characterization of spectra under open boundary conditions (OBC). Willis media provide a rigorous theoretical framework for modeling both frequency and spatial dispersion in elastic continua, which makes them promising candidates for defining spectral winding numbers and characterizing skin modes in non-Hermitian systems. Nevertheless, the application of Willis theory to active, non-Hermitian systems, and particularly to the formulation of generalized bulk-boundary correspondences and non-Bloch band theory, remains largely unexplored.

In this work, we develop a nonlocal, non-Hermitia Willis effective model to describe the global dynamic behavior of active metabeams. By employing dynamic source-driven homogenization, we establish a rigorous link between microscopic active scatterers and macroscopic constitutive relations. These scatterers, realized through sensor-actuator pairs with programmable transfer functions, enable tunable, directional, and frequency-dependent interactions. The resulting Willis model is validated against full-scale simulations of the microstructured beam, demonstrating excellent agreement with both the real and imaginary components of the dispersion relations across the full Brillouin zone. The model accurately captures a range of distinctive non-Hermitian wave phenomena, including low-frequency shear-enhanced flexural modes, strong nonreciprocity, and skin modes under OBC. To further understand the spectral topology, we perform an asymptotic analysis to construct a non-Bloch band theory, which facilitates analytical computation of the GBZ and establishes a bulk-boundary correspondence that directly connects spectral winding numbers to the localization direction and intensity of skin modes. Notably, this framework provides a closed-form analytical pathway that bypasses the need for numerical GBZ reconstruction, offering a predictive, tunable, and efficient tool for the design and analysis of non-Hermitian metamaterials based on extended Willis dynamics.

2. Dynamic homogenization of the metabeam with active scatterers

In this section, we develop a dynamic homogenization framework for a metabeam composed of periodically distributed active or self-sensing scatterers, as illustrated in Fig. 1(a). To capture Willis coupling effects, we assume that these active elements generate generalized symmetric and asymmetric loads-such as linear moments and velocities-in response to locally sensed fields, enabling programmable scattering behavior. Each scatterer is modeled as a point source governed by a local polarizability tensor within the Timoshenko beam theory (Fig. 1(d)), and interacts with others through long-range multiple scattering (Fig. 1(e)). Because the active elements exert controlled force and torque inputs, each scatterer effectively serves as a localized source of linear and angular momentum as well as mechanical energy. Under external excitation, the total wave field is decomposed into the background field in the host beam (Fig. 1(b)) and the combined local and multiple scattering fields from the active elements (Fig. 1(c)), yielding a dynamic Willis effective beam that captures the collective macroscopic response (Fig. 1(f)). Note that passive scattering are ignored as they are of significantly lower amplitude than the actively scattered fields, due to the deep subwavelength geometry of active scatterers. The homogenization procedure begins with the Timoshenko beam equations, which serve as the theoretical foundation (Section 2.1). It is important to mention that the scattering properties of the active scatterer presented here cannot be properly captured using the simple Euler beam theory because it lacks the degrees of freedom associated with Willis coupling. Section 2.2 discusses the metabeam response that combines both microscale local behavior and mesoscale multiple scattering. Section 2.3 presents the derivation of the

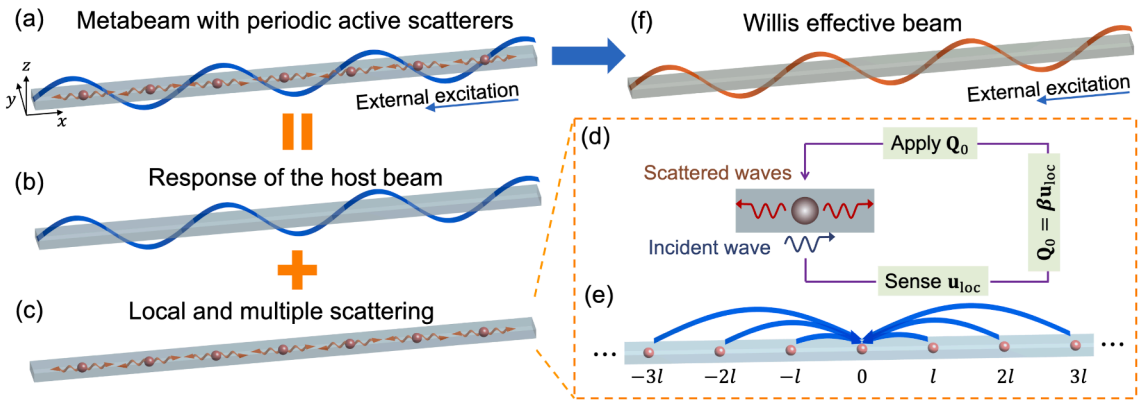

Fig. 1. Schematic of dynamic Willis homogenization in an active metabeam system. (a) A metabeam with periodically embedded active scatterers, subjected to external excitation. (b)-(c) The total response comprises the intrinsic response of the host beam (b) and the local plus multiple scattering effects introduced by the active elements (c). (d) Each active scatterer senses the local field vector $\mathbf{u}_{\text{loc}}$ and generates a generalized actuation vector $\mathbf{Q}_0 = \boldsymbol{\beta}\mathbf{u}_{\text{loc}}$, enabling programmable active scattering. (e) Illustration of multiple scattering across the array. (f) The metabeam and active scatterers in (a) are homogenized into a Willis effective beam via Willis homogenization framework.

effective constitutive relations. Finally, Section 2.4 formulates the nonlocal governing equations and the associated boundary value problem (BVP).

2.1. General equations of the Timoshenko beam

Consider a Timoshenko beam characterized by mass density ρ, Young's modulus E, and shear modulus G. The bending curvature κ, shear strain γ, rotational angle ψ, and transverse displacement w satisfy the following geometric relations

$$\begin{aligned} \kappa &= \partial_x \psi + p, \\ \gamma &= \partial_x w - \psi + s, \end{aligned} \tag{1}$$

where p and s represent the external curvature load and shear load, respectively. The material's response is governed by the balance of linear momentum μ and angular momentum J (Yao et al., 2009; Chen et al., 2020)

$$\begin{aligned} \partial_t \mu &= \partial_x F - f, \\ \partial_t J &= \partial_x M + F - q, \end{aligned} \tag{2}$$

where F denotes the shear force, M represents the bending moment, and f and q correspond to the transverse body force and external body torque, respectively. The general constitutive relation of the Timoshenko beam is given by Yao et al. (2009), Chen et al. (2020)

$$\begin{bmatrix} \kappa \\ \gamma \\ \mu \\ J \end{bmatrix} = \begin{bmatrix} 1/D_0 & 0 & 0 & 0 \\ 0 & 1/G_0 & 0 & 0 \\ 0 & 0 & \rho_0 & 0 \\ 0 & 0 & 0 & I_0 \end{bmatrix} \begin{bmatrix} M \\ F \\ \partial_t w \\ \partial_t \psi \end{bmatrix}, \tag{3}$$

where D_0 is the bending stiffness, G_0 is the shear stiffness, I_0 is the moment of inertia, and ρ_0 is the line mass density. These parameters are defined as $D_0 = EI$, $G_0 = k_s AG$, $I_0 = \rho I$, and $\rho_0 = \rho A$, where A is the cross-sectional area, k_s is the Timoshenko shear coefficient (taken as 5/6), I is the second moment of area, and ρ is the material density. In frequency-wavenumber domain $e^{i(kx-\omega t)}$, the general governing equations can be written in matrix form for the state vector

$$\boldsymbol{\zeta}(\omega, k)\mathbf{u} = \mathbf{Q}, \tag{4}$$

where

$$\boldsymbol{\zeta} = \begin{bmatrix} 1/D_0 & 0 & 0 & -ik \\ 0 & 1/G_0 & -ik & 1 \\ 0 & ik & \omega^2 \rho_0 & 0 \\ ik & 1 & 0 & \omega^2 I_0 \end{bmatrix}, \quad \mathbf{u} = \begin{bmatrix} M \\ F \\ w \\ \psi \end{bmatrix}, \quad \mathbf{Q} = \begin{bmatrix} p \\ s \\ f \\ q \end{bmatrix}, \tag{5}$$

where $\boldsymbol{\zeta}$ denotes the operator appearing in the governing equations of the Timoshenko beam, $\mathbf{u}$ is the state vector representing the beam's generalized degrees of freedom, and $\mathbf{Q}$ is the actuation vector representing the applied external loading. Moreover, the $\boldsymbol{\zeta}$ satisfies the following symmetry conditions:

$$\boldsymbol{\zeta}(\omega, k) = \boldsymbol{\zeta}^*(-\omega, -k), \quad \boldsymbol{\zeta}(\omega, k) = \boldsymbol{\zeta}^T(-\omega, -k), \quad \boldsymbol{\zeta}(\omega, k) = \boldsymbol{\zeta}(-\omega, k). \tag{6}$$

Under the incident wave, as illustrated in the top panel of Fig. 1(b), the general equations of the homogeneous host beam can be expressed in the state vector as

$$\boldsymbol{\zeta}\mathbf{u}_{\mathrm{h}} = \mathbf{Q}_{\mathrm{ext}}, \tag{7}$$

where $\mathbf{u}_{\mathrm{h}}$ denotes the incident response of the host beam, and $\mathbf{Q}_{\mathrm{ext}}$ indicates the incident excitation.

2.2. Response of the metabeam with active scatterers

For the active beam with periodically distributed scatterers under the incident excitation, as illustrated in the middle panel of Fig. 1(a), the total scattering wave field consists of two parts: (i) the local scattering generated by the active scatterers (Fig. 1(d)), and (ii) the multiple scattering effects resulting from their periodic arrangement (Fig. 1(e)). The active scatterers in Fig. 1(d) detect the local state vector $\mathbf{u}_{\mathrm{loc}}$ and generate the actuation vector $\mathbf{Q}_0$ to the beam. In the frequency domain, the local actuation vector is related to the local state vector through the polarizability tensor as shown in Fig. 1(d) (Chen et al., 2020),

$$\mathbf{Q}_0 = \boldsymbol{\beta}(\omega)\mathbf{u}_{\mathrm{loc}}, \tag{8}$$

where the tensor $\boldsymbol{\beta}(\omega)$ represents a frequency-dependent polarizability tensor with the component β_{ij} being an ith actuated loading Q_0^i by the active scatterer in response to a jth sensing field u_{loc}^j. For example, β_{11} indicates that the active scatterer excites a curvature load p in response to a sensed bending moment field M_{loc}, while β_{21} corresponds to a shear load s induced by the same input field. By leveraging circuit-based control, each element of the local constitutive matrix can be independently modulated, enabling the implementation of arbitrary frequency-dependent responses-including positive or negative values, real or imaginary components, and non-Hermitian configurations. Consequently, the macroscopic constitutive relations-derived through homogenization and governed by the polarizability tensor-inherit their tunability and complexity directly from the microscale response. By selecting appropriate elements of $\boldsymbol{\beta}(\omega)$, one can prescribe desired macroscopic behaviors, including non-Hermitian, frequency-dispersive, symmetry broken, and nonreciprocal effects.

Next, the multiple scattering theory is then implemented to study the multiple scattering from the periodically distributed active scatterers, as illustrated on Fig. 1(e) (Wang et al., 1993; Leung and Qiu, 1993; Liu et al., 2000; Martin, 2006). The state vector response at position x due to a point source $\mathbf{Q}(x') = \delta(x' - nL)\mathbf{Q}_n$ located at $x' = nL$ is given by

$$\mathbf{u}(x) = \mathbf{G}(\omega, x - nL)\mathbf{Q}_n. \tag{9}$$

where Green's function $\mathbf{G}$ in the frequency domain is derived in Appendix A. Applying the Bloch's theorem to the actuation vector $\mathbf{Q}_n$ (Sieck et al., 2017), we have

$$\mathbf{Q}_n = e^{iknL}\mathbf{Q}_0, \tag{10}$$

Therefore, the total local field $\mathbf{u}_{\mathrm{loc}}$ at $x = 0$ is the superposition of the local fields generated by active scatterers and the incident field of the host beam $\mathbf{u}_{\mathrm{h}}$

$$\mathbf{u}_{\mathrm{loc}} = \mathbf{u}_{\mathrm{h}} + \sum_{n\in\mathbb{Z}} \mathbf{G}(\omega, 0 - nL)\mathbf{Q}_n = \mathbf{u}_{\mathrm{h}} + \tilde{\mathbf{S}}(\omega, k)\mathbf{Q}_0, \tag{11}$$

where the scattering matrix is defined as

$$\tilde{\mathbf{S}}(\omega, k) = \sum_{n\in\mathbb{Z}} \mathbf{G}(\omega, 0 - nL)e^{iknL}. \tag{12}$$

By applying the symmetry condition of the Green's function in Eq. (A.16), we find that the scattering matrix $\tilde{\mathbf{S}}$ satisfies the following symmetry properties:

$$\tilde{\mathbf{S}}(\omega, k) = \tilde{\mathbf{S}}^*(-\omega, -k), \quad \tilde{\mathbf{S}}(\omega, k) = \tilde{\mathbf{S}}^T(-\omega, -k), \quad \tilde{\mathbf{S}}(\omega, k) = \tilde{\mathbf{S}}(-\omega, k). \tag{13}$$

Applying Bloch's theorem to the actuation vector $\mathbf{Q}_n$ in Eq. (10), the multiple scattering matrix becomes (Sieck et al., 2017; Shore and Yaghjian, 2007)

$$\begin{aligned}
\tilde{\mathbf{S}}(\omega, k) =& \sum_{n\in\mathbb{Z}} \left[\mathbf{R}_1(-nL)\mathbf{B}_1(-nL)^T e^{-i|nL|k_1} e^{iknL} + \mathbf{R}_2(-nL)\mathbf{B}_2(-nL)^T e^{-|nL|k_2} e^{iknL}\right] \\
=& \mathbf{R}_1(1)\mathbf{B}_1(1)^T \left(\frac{e^{-iL(k_1+k)}}{1 - e^{-iL(k_1+k)}} + \frac{1}{2}\right) + \mathbf{R}_1(-1)\mathbf{B}_1(-1)^T \left(\frac{e^{iL(k-k_1)}}{1 - e^{iL(k-k_1)}} + \frac{1}{2}\right) \\
&+ \mathbf{R}_2(1)\mathbf{B}_2(1)^T \left(\frac{e^{-L(k_2+ik)}}{1 - e^{-L(k_2+ik)}} + \frac{1}{2}\right) + \mathbf{R}_2(-1)\mathbf{B}_2(-1)^T \left(\frac{e^{L(ik-k_2)}}{1 - e^{L(ik-k_2)}} + \frac{1}{2}\right),
\end{aligned} \tag{14}$$

where $\mathbf{R}_1(x)$, $\mathbf{R}_2(x)$, $\mathbf{B}_1(x)$, and $\mathbf{B}_2(x)$ are given in Appendix A and only depend on the sign of the spatial coordinate x.

2.3. Homogenization method towards the Willis effective beams

Following the source-driven homogenization theory, the homogenization method of the active beam is presented, where the actuation vector is represented by an effective actuation vector $\mathbf{Q}_{\text{eff}}$, as shown in the bottom panel of Fig. 1(b). Following Eq. (4) in the beam, the governing equations of the homogenized active beam in the state vector are then given by

$$\boldsymbol{\zeta}\mathbf{u}_{\text{eff}} + \mathbf{Q}_{\text{eff}} = \mathbf{Q}_{\text{ext}}. \tag{15}$$

where $\mathbf{u}_{\text{eff}}$ denotes the effective field that incorporates the responses of both the host beam and the active scatterers. This effective field plays the same role as the unit-cell-averaged field in classical homogenization, but here it is introduced as an unknown vector to be determined, following Sieck et al. (2017). The rationale for introducing $\mathbf{u}_{\text{eff}}$ is fully consistent with the Willis framework and related homogenization studies (Willis, 2011; Alù, 2011; Nassar et al., 2015; Norris et al., 2012): our effective field can be regarded as equivalent to the ensemble-averaged field commonly used in Willis-type formulations (Willis, 2011; Nassar et al., 2015). Plus, $\mathbf{Q}_{\text{eff}}$ is an unknown actuation vector that depends on the local and multiple scattering waves of the active scatterers to be determined in the following.

In addition, the effective actuation vector $\mathbf{Q}_{\text{eff}}$ relates to the microscopic point actuation vector $\mathbf{Q}_0$ at $x = 0$ by applying spatial averaging as (Sieck et al., 2017; Chen et al., 2020; Alù, 2011)

$$\mathbf{Q}_{\text{eff}} = \frac{1}{l}\int_{-l/2}^{l/2} \delta(x)\mathbf{Q}_0\, dx = \frac{\mathbf{Q}_0}{l}, \tag{16}$$

where l is the unit cell length. Specifically, $\mathbf{Q}_{\text{eff}}$ is a distributed load density (force or moment per unit length), whereas $\mathbf{Q}_0$ is a concentrated load. Here, a point-source approximation is used, which is valid only when the unit-cell length scale exceeds the near-field region of the scattered wave. As illustrated in Fig. F.13, the near-field pattern generated by the extended actuator differs from that of an ideal point source in a small neighborhood of the actuator. To confine this mismatch within a single cell, the unit-cell size must be chosen larger than the near-field region, so that the macroscopic description samples only the far-field-like part of the scattered wave. In our design this condition is satisfied, but it also implies that the unit cell cannot be made arbitrarily small: Eq. (16) does not resolve sub-cell spatial variations of $\mathbf{Q}_0(x)$, and its validity is restricted to regimes where the actuator can be treated as effectively point-like at the scale of the homogenized beam.

It is worth noting that Eq. (7) is not an alternative to Eq. (15) but the microscopic equation that generates the host background field entering the scattering problem. Eq. (15) belongs to the homogenized description obtained from Eqs. (7), (8), (11), (15) and (16), and therefore cannot, by itself, serve as the sole starting point for obtaining the effective constitutive relations. Using Eqs. (7), (8), (11), (15) and (16), we then derive the effective constitutive relation, with detailed steps provided in the Appendix B.

$$\mathbf{Q}_{\text{eff}} = \mathbf{K}\mathbf{u}_{\text{eff}}, \tag{17}$$

where $\mathbf{K}$ is the macroscopic polarizability tensor satisfying

$$\mathbf{K} = \left[l\mathbf{I} - l\boldsymbol{\beta}\tilde{\mathbf{S}} - \boldsymbol{\beta}\boldsymbol{\zeta}^{-1}\right]^{-1}\boldsymbol{\beta}. \tag{18}$$

For the source-driven formulation, the effective constitutive coefficients are uniquely determined and independent of the particular excitation once the polarization are specified, in contrast to source-free or retrieval-based descriptions (Alù, 2011; Sieck et al., 2017). Therefore, Eqs. (7), (8), (11), (15), and (16) are inhomogeneous and admit unique solutions, so the macroscopic polarizability tensor is uniquely determined. If $\boldsymbol{\beta}$ is nonsingular, Eq. (18) simplifies to

$$\mathbf{K} = \left[l\boldsymbol{\beta}^{-1} - l\tilde{\mathbf{S}} - \boldsymbol{\zeta}^{-1}\right]^{-1}. \tag{19}$$

The macroscopic polarizability tensor $\mathbf{K}(\omega, k)$ depends on both frequency and wavenumber. Each element K_{ij} characterizes the generation of an effective source component Q^i_{eff} by the effective medium in response to an effective field component u^j_{eff}. For instance, K_{11} indicates that the effective medium generates a curvature p_{eff} in response to an effective bending moment M_{eff}, while K_{21} corresponds to an effective shear s_{eff} induced by the same bending moment field. In general, each element K_{ij} of the macroscopic polarizability tensor is directly related to the corresponding element β_{ij} of the local polarizability tensor. To realize a nonzero K_{ij}, it is necessary to implement a nonzero β_{ij} at the microscopic level.

Meanwhile, the symmetry properties of the macroscopic polarizability tensor $\mathbf{K}(\omega, k)$ are governed by those of the microscopic polarizability tensor $\boldsymbol{\beta}(\omega)$. In this study, the microscopic tensor $\boldsymbol{\beta}(\omega)$ breaks a key symmetry condition:

$$\boldsymbol{\beta}(\omega) \neq \boldsymbol{\beta}^T(-\omega), \tag{20}$$

while preserving the real-valued condition and time-reversal symmetry:

$$\boldsymbol{\beta}(\omega) = \boldsymbol{\beta}^*(-\omega), \quad \boldsymbol{\beta}(\omega) = \boldsymbol{\beta}(-\omega). \tag{21}$$

Given the symmetry conditions of the homogenized stiffness operator $\boldsymbol{\zeta}(\omega, k)$ in Eq. (6) and the scattering matrix $\tilde{\mathbf{S}}(\omega, k)$ in Eq. (13), the macroscopic polarizability tensor $\mathbf{K}(\omega, k)$ inherits the following properties:

$$\mathbf{K}(\omega, k) = \mathbf{K}^*(-\omega, -k), \quad \mathbf{K}(\omega, k) \neq \mathbf{K}^T(-\omega, -k), \quad \mathbf{K}(\omega, k) = \mathbf{K}(-\omega, k), \tag{22}$$

Substituting Eq. (17) into Eq. (15) in the absence of the incident wave and comparing it with Eq. (3), we obtain a general constitutive relation of the active metabeams in the matrix form

$$\begin{bmatrix} \kappa_{\text{eff}} \\ \gamma_{\text{eff}} \\ \mu_{\text{eff}} \\ J_{\text{eff}} \end{bmatrix} = \begin{bmatrix} 1/D_0 + K_{11} & K_{12} & K_{13}/(-i\omega) & K_{14}/(-i\omega) \\ K_{21} & 1/G_0 + K_{22} & K_{23}/(-i\omega) & K_{24}/(-i\omega) \\ K_{31}/(-i\omega) & K_{32}/(-i\omega) & \rho_0 + K_{33}/(-\omega^2) & K_{34}/(-\omega^2) \\ K_{41}/(-i\omega) & K_{42}/(-i\omega) & K_{43}/(-\omega^2) & I_0 + K_{44}/(-\omega^2) \end{bmatrix} \begin{bmatrix} M_{\text{eff}} \\ F_{\text{eff}} \\ v_{\text{eff}} \\ \varphi_{\text{eff}} \end{bmatrix}, \tag{23}$$

where v_{eff} and φ_{eff} represent the velocity and angular velocity, respectively, satisfying $v_{\text{eff}} = \dot{w}_{\text{eff}}$ and $\varphi_{\text{eff}} = \dot{\psi}_{\text{eff}}$ in the time domain, and $v_{\text{eff}} = -i\omega w_{\text{eff}}$ and $\varphi_{\text{eff}} = -i\omega\psi_{\text{eff}}$ in the frequency domain. When $\boldsymbol{\beta} = \mathbf{0}$, the macroscopic polarizability $\mathbf{K}$ also vanishes, and the effective constitutive relations reduce to the diagonal form corresponding to a classical Timoshenko beam. Using these relations, we rewrite Eq. (23) in the Willis-type effective constitutive relations as

$$\begin{bmatrix} \boldsymbol{\varepsilon} \\ \mathbf{p} \end{bmatrix} = \begin{bmatrix} \mathbf{S} & \mathbf{B} \\ \mathbf{D} & \boldsymbol{\rho} \end{bmatrix} \begin{bmatrix} \boldsymbol{\sigma} \\ \mathbf{v} \end{bmatrix} \tag{24}$$

where

$$\boldsymbol{\varepsilon} = \begin{bmatrix} \kappa_{\text{eff}} \\ \gamma_{\text{eff}} \end{bmatrix}, \mathbf{p} = \begin{bmatrix} \mu_{\text{eff}} \\ J_{\text{eff}} \end{bmatrix}, \boldsymbol{\sigma} = \begin{bmatrix} M_{\text{eff}} \\ F_{\text{eff}} \end{bmatrix}, \mathbf{v} = \begin{bmatrix} v_{\text{eff}} \\ \varphi_{\text{eff}} \end{bmatrix}, \tag{25}$$

and

$$\begin{aligned} \mathbf{S} &= \begin{bmatrix} -1/D_0 + K_{11} & K_{12} \\ K_{21} & 1/G_0 + K_{22} \end{bmatrix}, \quad \mathbf{B} = \begin{bmatrix} K_{13}/(-i\omega) & K_{14}/(-i\omega) \\ K_{23}/(-i\omega) & K_{24}/(-i\omega) \end{bmatrix}, \\ \mathbf{D} &= \begin{bmatrix} K_{31}/(-i\omega) & K_{32}/(-i\omega) \\ K_{33}/(-i\omega) & K_{34}/(-i\omega) \end{bmatrix}, \quad \boldsymbol{\rho} = \begin{bmatrix} \rho_0 + K_{33}/(-\omega^2) & K_{34}/(-\omega^2) \\ K_{43}/(-\omega^2) & I_0 + K_{44}/(-\omega^2) \end{bmatrix}. \end{aligned} \tag{26}$$

where $\mathbf{S}$ and $\boldsymbol{\rho}$ denotes as the effective stiffness and density tensors of the active metabeam, and $\mathbf{B}$ and $\mathbf{D}$ are the Willis coupling tensors. In previous studies (Willis, 2011; Nassar et al., 2015), the constitutive relation in Eq. (24) is not unique in the periodic case, because the macroscopic kinematic fields (strain and velocity) are both derived from the same displacement field. Introducing an eigenstrain makes strain and velocity independent and restores uniqueness; once the eigenstrain is specified, a unique set of Willis constitutive relations follows. Our source-driven formulation, in which the constitutive relation is unique, can be interpreted as working in a particular eigenstrain gauge $\gamma = 0$: the effective fields play the role of eigenstrain-fixed variables, and no additional eigenstrain field is introduced explicitly. In this sense, our results correspond to one specific, well-defined choice of eigenstrain, and the resulting Willis parameters are uniquely determined by the hierarchical model. Based on the symmetry properties of the polarization tensor $\mathbf{K}(\omega)$ in Eq. (22), the effective constitutive tensors satisfy the real-valued conditions

$$\mathbf{S}(\omega, k) = \mathbf{S}^*(-\omega, -k), \quad \mathbf{B}(\omega, k) = \mathbf{B}^*(-\omega, -k), \quad \mathbf{D}(\omega, k) = \mathbf{D}^*(-\omega, -k), \quad \boldsymbol{\rho}(\omega, k) = \boldsymbol{\rho}^*(-\omega, -k), \tag{27}$$

the time-reversal symmetry

$$\mathbf{S}(\omega, k) = \mathbf{S}(-\omega, k), \quad \mathbf{B}(\omega, k) = -\mathbf{B}(-\omega, k), \quad \mathbf{D}(\omega, k) = -\mathbf{D}(-\omega, k), \quad \boldsymbol{\rho}(\omega, k) = \boldsymbol{\rho}(-\omega, k), \tag{28}$$

and the violation of major symmetry

$$\mathbf{S}(\omega, k) \neq \mathbf{S}^T(-\omega, -k), \quad \mathbf{B}(\omega, k) \neq -\mathbf{D}^T(-\omega, -k), \quad \boldsymbol{\rho}(\omega, k) \neq \boldsymbol{\rho}^T(-\omega, -k). \tag{29}$$

Furthermore, combining Eq. (28) and Eq. (29) leads to the violation of Maxwell-Betti reciprocity

$$\mathbf{S}(\omega, k) \neq \mathbf{S}^T(\omega, -k), \quad \mathbf{B}(\omega, k) \neq \mathbf{D}^T(\omega, -k), \quad \boldsymbol{\rho}(\omega, k) \neq \boldsymbol{\rho}^T(\omega, -k). \tag{30}$$

In our study, the asymmetry of the effective compliance and Willis matrices originates from the asymmetry of the local polarizability tensor in Eq. (20). Physically, a non-symmetric $\boldsymbol{\beta}$ means that different components of the local state $\mathbf{u}_{\text{loc}}$ drive the actuator $\mathbf{Q}_0$ in an unbalanced way, so that the response in one direction is not reciprocally matched by the conjugate direction; this lack of balance manifests, after homogenization, as asymmetric elastic and Willis couplings. By contrast, the effective density tensor governs the relation between generalized momentum and velocity, and within the present point-actuator model do not directly implement such momentum-velocity cross couplings. As a result, an asymmetric density tensor cannot be generated solely through $\boldsymbol{\beta}$ and instead requires dedicated inertial mechanisms, such as those realized in our previous work on odd density media (Wu et al., 2023). To preserve a Hermitian effective description, one must enforce the symmetry condition in Eq. (20), which yields symmetric effective constitutive tensors.

Meanwhile, to clarify the role of spatial symmetry, we carry out a parity analysis of the effective constitutive matrix (see Appendix G). In one dimension, parity corresponds to the inversion $x \to -x$ (or $k \to -k$ in reciprocal space). In general, the breakdown of parity symmetry is accompanied by the breakdown of the major symmetry conditions summarized in Fig. 2, because violating major symmetry requires nonreciprocal couplings, which also break momentum-inversion symmetry. In our active metabeam, the sensor–actuator feedback produces a nonzero $\beta_{21}(\omega)$, which breaks the microscopic parity condition in Eq. (G.12). This asymmetry propagates to the macroscopic constitutive tensor, leading to broken parity symmetry and major symmetry.

The effective constitutive matrix in Eq. (24) depends on both frequency and wavenumber and thus encodes temporal and spatial nonlocality. Nevertheless, the underlying medium remains causal: the response kernel in Eq. (24) vanishes for $t < 0$ and outside the

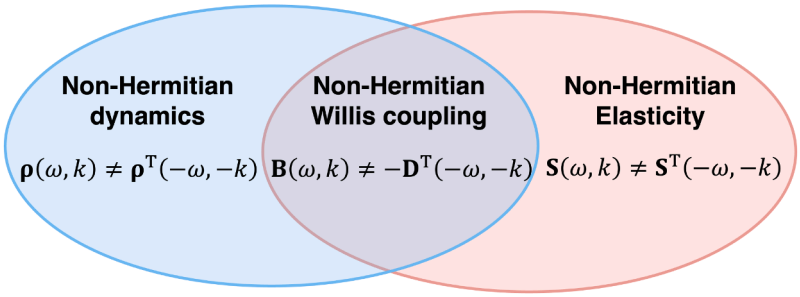

Fig. 2. Possible constitutive operators in elastodynamics with broken major symmetry. The broken major symmetry of the elastic tensor $\mathbf{C}(\omega,k) \neq \mathbf{C}^{T}(-\omega,-k)$, density tensor $\boldsymbol{\rho}(\omega,k) \neq \boldsymbol{\rho}^{T}(-\omega,-k)$, and Willis coupling tensor $\mathbf{B}(\omega,k) \neq -\mathbf{D}^{T}(-\omega,-k)$ leads to the non-hermitian media.

causal cone $|x| > ct$, where c is the maximal group velocity of the Timoshenko beam. As shown in Appendix H, this causal support implies that $\boldsymbol{S}(\omega,k)$ is analytic in the upper half of the complex ω-plane for fixed k, and the real and imaginary parts of $\boldsymbol{S}(\omega,k)$ are linked by a wavenumber-dependent Kramers-Kronig relation. In the limit $c \to \infty$, these expressions reduce to the standard frequency-only Kramers-Kronig formulas, recovering the usual Hilbert-transform relation between the real and imaginary parts of the effective moduli.

Eqs. (27), (28), and (29) serve as the fundamental symmetry constraints in the macroscopic description, while Eq. (30) can be derived from them. Eq. (27) reflects the requirement that all physical fields in classical physics must be real-valued (Agranovich and Ginzburg, 2013; Shokri and Rukhadze, 2019). Eq. (28) expresses time-reversal symmetry (Agranovich and Ginzburg, 2013; Shokri and Rukhadze, 2019; Altman and Suchy, 2011). Moreover, Eq. (29) captures the breaking of major symmetry in the Willis effective model. This broken major symmetry highlights the inherently non-Hermitian nature of Willis beams, as illustrated in Fig. 2. Finally, Eq. (30) corresponds to the violation of the Maxwell-Betti reciprocity theorem, which results from the combined breaking of major and time-reversal symmetries (Agranovich and Ginzburg, 2013; Shokri and Rukhadze, 2019; Pernas-Salomón and Shmuel, 2020b).

In our study, the asymmetry of the effective compliance and Willis matrices originates from the asymmetry of the local polarizability tensor in Eq. (20). Physically, a non-symmetric $\boldsymbol{\beta}$ means that different components of the local state $\mathbf{u}_{\mathrm{loc}}$ drive the actuator $\mathbf{Q}_0$ in an unbalanced way, so that the response in one direction is not reciprocally matched by the conjugate direction; this lack of balance manifests, after homogenization, as asymmetric elastic and Willis couplings. By contrast, the effective density tensor governs the relation between generalized momentum and velocity, and within the present point-actuator model does not directly implement such momentum-velocity cross couplings. As a result, an asymmetric density tensor cannot be generated solely through $\boldsymbol{\beta}$ and instead requires dedicated inertial mechanisms, such as those realized in our previous work on odd density media (Wu et al., 2023). To preserve a Hermitian effective description, one must enforce the symmetry condition in Eq. (20), which yields symmetric effective constitutive tensors.

Here, material properties depend on both frequency and wavenumber, indicating that the Willis effective metabeam exhibits both frequency and spatial dispersion (Agranovich and Ginzburg, 2013). Frequency and wavenumber are treated as independent variables, as discussed in Appendix C. In the space and time domains, the constitutive relations are expressed in the convolution form as (Agranovich and Ginzburg, 2013; Jackson, 2012; Pernas-Salomón and Shmuel, 2020a).

$$\begin{bmatrix} \boldsymbol{\epsilon}(t,x) \\ \mathbf{p}(t,x) \end{bmatrix} = \int_{-\infty}^{t}\int_{-\infty}^{\infty} \begin{bmatrix} \mathbf{S}(t,t';x,x') & \mathbf{B}(t,t';x,x') \\ \mathbf{D}(t,t';x,x') & \boldsymbol{\rho}(t,t';x,x') \end{bmatrix} \begin{bmatrix} \boldsymbol{\sigma}(t',x') \\ \mathbf{v}(t',x') \end{bmatrix} dt'dx' \tag{31}$$

If the medium's properties remain constant over time (time-independent), translational symmetry in the time domain is preserved, making the constitutive relation dependent only on the time difference $t-t'$ (Agranovich and Ginzburg, 2013). Similarly, if the medium is spatially uniform, the constitutive relation depends only on the spatial difference $x-x'$ (Agranovich and Ginzburg, 2013). In summary, we obtain

$$\begin{bmatrix} \boldsymbol{\epsilon}(t,x) \\ \mathbf{p}(t,x) \end{bmatrix} = \int_{-\infty}^{t}\int_{-\infty}^{\infty} \begin{bmatrix} \mathbf{S}(t-t',x-x') & \mathbf{B}(t-t',x-x') \\ \mathbf{D}(t-t',x-x') & \boldsymbol{\rho}(t-t',x-x') \end{bmatrix} \begin{bmatrix} \boldsymbol{\sigma}(t',x') \\ \mathbf{v}(t',x') \end{bmatrix} dt'dx' \tag{32}$$

2.4. Governing equations and the boundary value problem of the Willis effective beam

For the Willis effective metabeam, the effective governing equations in the space-time domain can be obtained by substituting the constitutive relation in Eq. (32) into the general governing equations in Eq. (2) and Eq. (1) as

$$\begin{aligned} &\begin{bmatrix} 0 & -\partial_x \\ -\partial_x & 1 \end{bmatrix} \boldsymbol{\sigma}(t,x) + \int_{-\infty}^{t}\int_{\infty}^{\infty} \mathbf{S}(t-t',x-x')\boldsymbol{\sigma}(t',x') + \mathbf{B}(t-t',x-x')\partial_t \mathbf{w}(t',x')dt'dx' = \mathbf{q}_1 \\ &\begin{bmatrix} 0 & \partial_x \\ \partial_x & 1 \end{bmatrix} \mathbf{w}(t,x) + \partial_t \int_{-\infty}^{t}\int_{\infty}^{\infty} \mathbf{D}(t-t',x-x')\boldsymbol{\sigma}(t',x') + \boldsymbol{\rho}(t-t',x-x')\partial_t \mathbf{w}(t',x')dt'dx' = \mathbf{q}_2 \end{aligned} \tag{33}$$

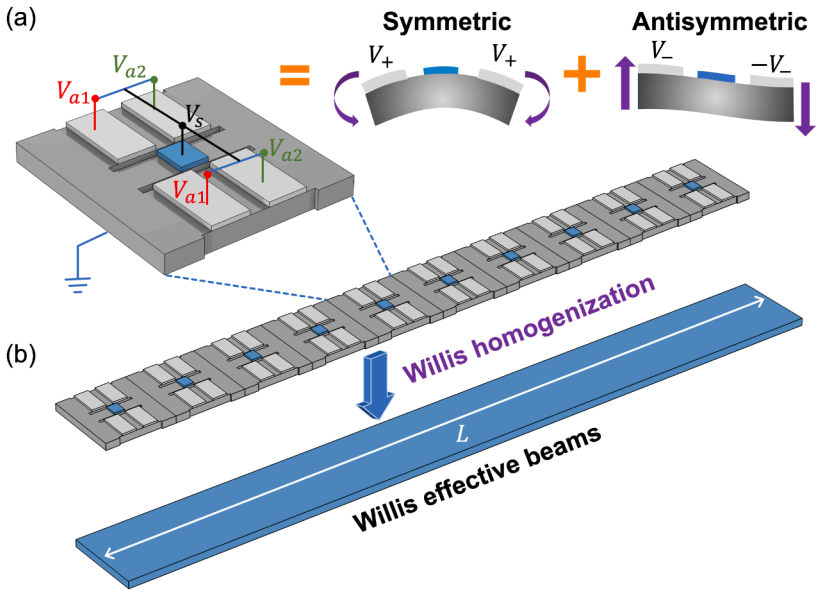

Fig. 3. Schematic of the metabeam architecture and its homogenization process. (a) Microstructure of a unit cell consisting of piezoelectric actuators and control circuitry. The output voltages $V_{a1} = H_1(\omega)V_s$ and $V_{a2} = H_2(\omega)V_s$ are generated from the input sensor voltage V_s through frequency-dependent transfer functions $H_1(\omega)$ and $H_2(\omega)$. For general actuator voltages, the input can be decomposed into symmetric $V_+ = (V_{a1} + V_{a2})/2$ and antisymmetric $V_- = (V_{a1} - V_{a2})/2$ components. The symmetric component produces bending curvature actuation, while the antisymmetric component generates shear strain actuation. (b) Periodic assembly of unit cells into a composite finite metabeam with length L (top panel). The macroscopic behavior is captured by a Willis effective beam (bottom panel) derived via Willis homogenization.

where $\mathbf{w} = [w, \psi]^T$, $\mathbf{q}_1 = [p_{\text{ext}}, s_{\text{ext}}]^T$, and $\mathbf{q}_2 = [f_{\text{ext}}, q_{\text{ext}}]^T$. In the frequency-wavenumber domain, the governing equations take the form

$$\mathbf{H}\mathbf{u}_{\text{eff}} = \mathbf{Q}_{\text{ext}}, \tag{34}$$

where

$$\mathbf{H} = \begin{bmatrix} 0 & 0 & 0 & -ik \\ 0 & 0 & -ik & 1 \\ 0 & ik & 0 & 0 \\ ik & 1 & 0 & 0 \end{bmatrix} + \begin{bmatrix} \mathbf{S} & -i\omega\mathbf{B} \\ -i\omega\mathbf{D} & -\omega^2\boldsymbol{\rho} \end{bmatrix}. \tag{35}$$

In this final form, $\mathbf{Q}_{\text{eff}}$ no longer appears explicitly on the right-hand side and is fully absorbed into the matrix $\mathbf{H}$. In the absence of an external source, the dispersion relations in terms of ω and k are obtained by setting the determinant of the coefficient matrix to zero

$$\det(\mathbf{H}) = 0. \tag{36}$$

and the corresponding solution $\mathbf{u}_{\text{eff}}$ in Eq. (34) represents the eigenvector.

For the finite boundary problem, boundary conditions are required to determine the eigenfrequencies and eigenmodes of the active metabeam. Based on the boundary conditions of the conventional Timoshenko beam, the most relevant boundary conditions for the Willis effective metabeam are

$$\begin{aligned} &\text{Fixed}: && w_{\text{eff}} = 0, \quad \psi_{\text{eff}} = 0 \\ &\text{Simply supported}: && w_{\text{eff}} = 0, \quad M_{\text{eff}} = 0 \\ &\text{Free}: && M_{\text{eff}} = 0, \quad F_{\text{eff}} = 0 \end{aligned} \tag{37}$$

In the Willis effective media, the bending moment, shear force, displacement, and rotational angle are integrated into a state vector, allowing them to be directly prescribed as boundary conditions. This approach eliminates the challenges of the conventional Willis media framework, which involves second-order derivatives. In the traditional formulation, the constitutive relations in Eq. (24) express the bending moment and shear force in terms of displacement and rotational angle, making their boundary conditions nonlocal. As a result, solving nonlocal boundary conditions analytically becomes intractable, requiring advanced numerical methods (Rabczuk et al., 2023). In the present state-vector formulation, these quantities are treated as independent components of the effective field, so all boundary variables are imposed locally at the boundary and no nonlocal scattering operators enter the boundary conditions.

A variational derivation for the boundary conditions is generally unavailable for odd elasticity and odd Willis media, where energy conservation is broken. In conventional elasticity, the existence of a strain-energy density ensures that the elastic tensor equals the

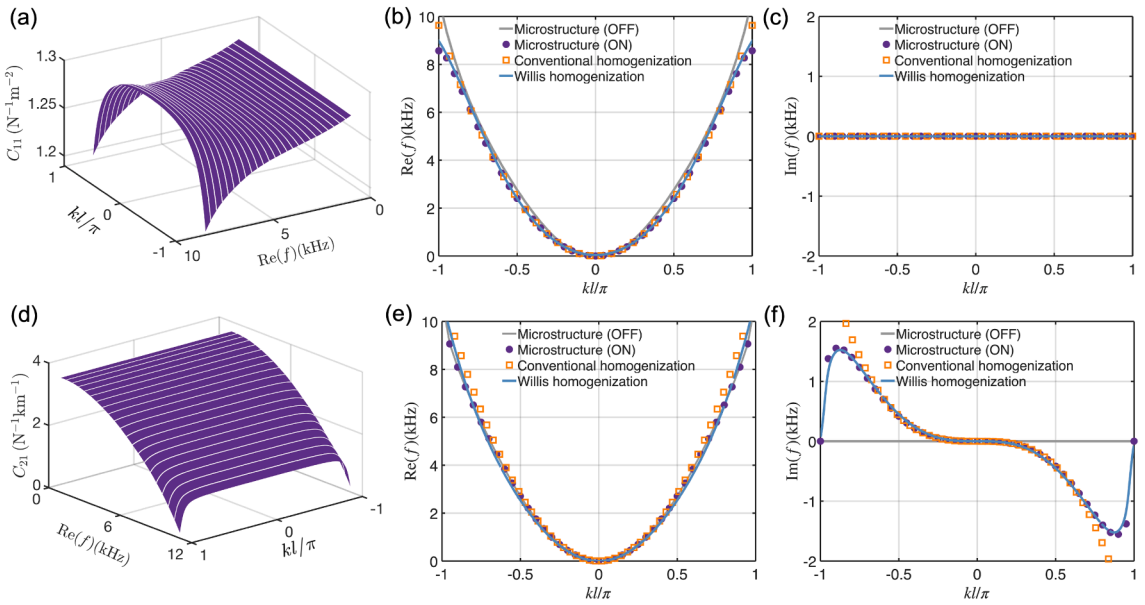

Fig. 4. Effective material properties and dispersion relations for symmetric and antisymmetric real transfer functions. (a-c) Symmetric case with $H_1(\omega) = H_2(\omega) = 0.05$: (a) The effective stiffness S_{11} as a function of frequency and wavenumber. (b) Real and (c) imaginary parts of the dispersion curves obtained from microstructure simulation without control (gray solid line), with control (purple dots), and predictions from the conventional effective model (orange squares) and Willis effective model (blue solid line). (d-f) Antisymmetric case with $H_1(\omega) = -H_2(\omega) = 0.3$: (d) The effective coupling S_{21} as a function of frequency and wavenumber. (e) Real and (f) imaginary parts of the dispersion curves under the same comparison conditions as in (b-c).

mixed second derivative of a potential function, which guarantees the major symmetry and provides a variational foundation for the boundary conditions. However, odd elasticity and odd Willis media involve non-symmetric constitutive matrices that cannot be derived from a scalar potential. Consequently, the associated variational principle remains an open question.

3. Microstructure design and validation of the Willis effective medium

The microstruture design of active metabeams is an important area of metamaterial research. Specifically, the ability to design active mechanical Willis scatterers that provide arbitrary control of the scattering polarizabilities is one of the fundamental challenges in further improving the ability to manipulate wavefronts over wide frequency ranges. In this section, an active Willis meta-beam is designed by introducing piezoelectric sensor-actuator-pairs controlled with digital circuits, where electrical transfer functions are encoded. The frequency-dependent polarizability tensor is then determined using a numerical retrieval approach based on the finite element simulations. Finally, the proposed homogenization method is validated by comparing its predicted dispersion relations with those obtained from the real microstructure under various transfer functions.

3.1. Microstructure design and its effective homogenization

To construct the mechanical Willis metabeam, an array of thin slits is introduced into a host beam, forming in each active scatterer a sensing beam and two actuating beams, as illustrated in Fig. 3(a). A piezoelectric sensor is bonded at the center of the sensing beam, while two pairs of piezoelectric actuators are symmetrically attached to the actuating beams. These actuators are electrically connected to a digital control system, with the two actuators on the left sharing an output voltage V_{a1}, and those on the right sharing V_{a2}. The sensor measures the local curvature of the sensing beam to detect incident waves, while the actuators generate programmed symmetric and antisymmetric scattered fields, as shown in Fig. 3(a). The control system establishes a functional relationship between the sensed signal and the actuation voltages through two frequency-dependent transfer functions:

$$\begin{aligned} V_{a1} &= H_1(\omega)V_s, \\ V_{a2} &= H_2(\omega)V_s, \end{aligned} \tag{38}$$

where the sensing voltage V_s is given by $V_s = \int_A D_z \, dA/C_0$, with A denoting the top surface area of the sensing piezoelectric patch, D_z the z-component of the electric displacement vector, and C_0 the capacitance defined in Appendix D.

In practice, the sensor records both the incident wave and the feedback response generated by the actuators. To isolate the incident wave, a mechanical feedback transfer function g is implemented in the control system (seeAppendix E for details). The output of g is subtracted from the raw sensor signal, yielding a corrected sensing voltage V_s that represents only the incident input. This signal

is then used to drive the actuators, forming a feedforward control loop. This feedforward architecture ensures stability and accurate realization of the desired transfer functions. The complete circuit design and theoretical validation of this scheme are provided in Appendix E.

The asymmetric actuation voltages V_{a1} and V_{a2} are decomposed into symmetric and antisymmetric components, as illustrated in Fig. 3(a). The symmetric component produces bending moment inputs, whereas the antisymmetric component generates shear forces. This microstructure design enables direct and independent control of nonzero elements β_{11} and β_{21} of the polarizability tensor. It should be noticed that the proposed design is mainly concentrated on bending curvature sensing and actuation in moment and shear channels, the approach can be extended and modified to access other actuation vectors to realize non-zero Willis coupling coefficients.

In general, a transfer function can be represented as a complex-valued rational function. For instance, the transfer functions $H_1(\omega)$ and $H_2(\omega)$ in this study can be written as

$$H_i(\omega) = \frac{\sum_{m=0}^{M} a_{m,i}\,\omega^m}{\sum_{n=0}^{N} b_{n,i}\,\omega^n}, \quad \text{for } i = 1, 2. \tag{39}$$

where M and N are the highest-order indices, and $a_{m,i}$ and $b_{n,i}$ are the complex coefficients of the mth and nth order terms in the numerator and denominator polynomials of $H_i(\omega)$, respectively. In fact, electrical transfer functions and mechanical polarizabilities are intrinsically related by the simplified expressions $\beta_{11} = \chi_1\left(\frac{H_1+H_2}{2}\right)$ and $\beta_{21} = \chi_2\left(\frac{H_1-H_2}{2}\right)$, where χ_1 and χ_2 denote rational functions describing the electromechanical coupling of symmetric and antisymmetric modes, respectively.

To determine $\boldsymbol{\beta}(\omega)$ for a given microstructure, we adopt a retrieval-based approach outlined in Appendix F. This method extracts the polarizability tensor numerically by combining local field measurements and scattered response data obtained from full-scale finite element simulations. Specifically, four independent scattering tests are performed, each yielding a distinct set of local state vectors and associated actuation vectors. These results are used to construct a linear system of 16 equations based on Eq. (8), enabling the unique determination of all 16 components of the polarizability tensor. The accuracy of this retrieval is validated by comparing the predicted scattered fields with those computed from direct numerical simulations, confirming the effectiveness of modeling the microstructure as a localized source governed by $\boldsymbol{\beta}(\omega)$. This retrieved tensor serves as the input to the homogenization framework, enabling a direct link between the microstructural configuration and the effective nonlocal constitutive response.

Under the Willis homogenization framework in Fig. 3(b), the nonzero components of the effective constitutive relation in Eq. (23) can be obtained as

$$\begin{aligned} S_{11} &= \frac{1}{D_0} + K_{11}, \\ S_{21} &= K_{21}, \end{aligned} \tag{40}$$

where

$$K_{11} = \frac{\beta_{11}\left(b_4k^4 + b_2k^2 + b_0\right)}{a_4k^4 + a_2k^2 + a_1k + a_0}, \quad K_{21} = \frac{\beta_{21}\left(b_4k^4 + b_2k^2 + b_0\right)}{a_4k^4 + a_2k^2 + a_1k + a_0}, \tag{41}$$

and the coefficients a_i and b_i are determined by the host beam parameters and the unit cell geometry:

$$\begin{aligned} b_4 &= -D_0\beta_{11}g_0 \\ b_2 &= \omega^2\left(D_0\rho_0 + I_0g_0\right) \\ b_0 &= \rho_0\omega^2\left(-I_0\omega^2 + g_0\right) \\ a_4 &= D_0lg_0\left(-1 + S_{12}\beta_{21} + S_{11}\beta_{11}\right) \\ a_2 &= -\omega^2\left(-D_0l\rho_0 - I_0lg_0 + D_0lS_{12}\beta_{21}\rho_0 + I_0lS_{12}\beta_{21}g_0 + D_0lS_{11}\beta_{11}\rho_0 + D_0I_0\beta_{11}g_0 + I_0lS_{11}\beta_{11}g_0\right) \\ a_1 &= -D_0\beta_{21}g_0\omega^2\rho_0 i \\ a_0 &= -\omega^2\rho_0\left(-I_0\omega^2 + g_0\right)\left(-l + lS_{12}\beta_{21} + D_0\beta_{11} + lS_{11}\beta_{11}\right). \end{aligned} \tag{42}$$

In Eq. (41), K_{11} and K_{21} are proportional to β_{11} and β_{21}, respectively, each scaled by a rational function. For a symmetric transfer function where $H_1(\omega) = H_2(\omega)$, the actuators generate only bending moments, making β_{11} the only nonzero component. Consequently, K_{11} is nonzero, modifying the effective bending stiffness. For an antisymmetric transfer function where $H_1(\omega) = -H_2(\omega)$, the actuators generate only shear strain, resulting in β_{21} as the only nonzero component. In this case, K_{21} becomes nonzero, leading to the formation of effective shear stiffness. For an asymmetric transfer function, where $H_1(\omega) \neq H_2(\omega)$ and $H_1(\omega) \neq -H_2(\omega)$, both K_{11} and K_{21} are nonzero. As $\omega \to 0$, Eq. (40) reduces to

$$\begin{aligned} S_{11} &= \frac{1}{D_0} + \frac{\beta_{11}}{l - D_0\beta_{11}}, \\ S_{21} &= \frac{\beta_{21}}{l - D_0\beta_{11}}, \end{aligned} \tag{43}$$

which corresponds to the conventional effective model in the low-frequency, long-wavelength regime. In this limit, multiple-scattering effects become negligible, the effective elastic constants are determined solely by the local polarizability tensor, and the Willis constitutive relation reduces to a local form.

3.2. Validation of Willis effective beams

This subsection focuses on the validation of the proposed Willis effective model, with an emphasis on the high-frequency dynamic regime where classical effective theories often fail. We investigate how nonreciprocal and non-Hermitian effects-induced by active microstructural elements-can be systematically captured through generalized homogenization. The Willis effective model is validated through direct comparison with the numerical simulations of the active beam with microstructures, enabling the continuum description in wave manipulation strategies. By bridging microstructure design and effective properties, this validation supports development of the active Willis media for tunable, programmable, and non-Hermitian wave control capabilities. The geometric parameters and material properties used in this subsection are provided in Appendix D.

For simplicity, we begin with an active beam employing symmetric transfer functions, $H_1(\omega) = H_2(\omega) = 0.05$. This configuration produces only bending actuation, resulting in a nonzero β_{11}, while all other components of the polarizability tensor remain zero. Since the symmetry condition in Eq. (20) is preserved, the system remains Hermitian. According to Eq. (40), only S_{11} is modified, and its real part is shown in Fig. 4(a); the imaginary part is negligibly small and thus omitted. The effective S_{11}, which depends on both frequency and wavenumber, is always greater than the inverse of the bending stiffness of the host beam $1/D_0$, indicating that the active elements reduce the effective bending stiffness of the metabeam. The dispersion curves from the microstructure with control OFF, the microstructure with control ON, the Willis effective model from Eq. (40), and the conventional model from Eq. (43) are illustrated in Fig. 4(b,c). Since β_{11} acts as a local bending source, it reduces the macroscopic bending stiffness, leading to a downward shift in the real part of the dispersion curve for the control ON case relative to the control OFF case, as shown in Fig. 4(b). Moreover, because the symmetric transfer functions preserve the symmetry condition, the major symmetry condition is also satisfied, ensuring Hermiticity and resulting in a purely real spectrum, as confirmed in Fig. 4(c). In addition, both S_{11} and the resulting dispersion curves are symmetric with respect to wavenumber, consistent with the preservation of the reciprocity condition. While the conventional model accurately captures the dispersion behavior only in the long-wavelength, low-frequency regime, the Willis effective model maintains excellent agreement across the entire Brillouin zone-highlighting the essential role of spatial dispersion in modeling high-frequency wave phenomena.

For antisymmetric transfer functions, $H_1(\omega) = -H_2(\omega) = 0.3$, the effective properties and dispersion relations are shown in Fig. 4(d-f). In this configuration, the active scatterers induce only shear deformation, leading to a nonzero S_{21} and the breakdown of the major symmetry condition in Eq. (29). The real part of S_{21} is shown, while its imaginary part remains negligible and is therefore omitted. Since the antisymmetric scatterers do not alter the bending stiffness, the real part of the dispersion curves for the microstructure with control ON remains nearly identical to that of the control OFF case. However, the emergence of S_{21} breaks Hermiticity, introducing a nonzero imaginary component into the dispersion relation. At the same time, the reciprocity condition in Eq. (30) is violated, making the imaginary part antisymmetric with respect to wavenumber. This asymmetry leads to attenuation of left-propagating waves (negative wavenumber) and amplification of right-propagating waves (positive wavenumber), thereby enabling nonreciprocal wave propagation. While the conventional model accurately predicts the imaginary part only in the long-wavelength regime, the Willis effective model maintains excellent agreement with the full-wave simulations across the entire Brillouin zone.

The Willis homogenization framework is now extended to consider the cases beyond constant transfer functions to accommodate frequency-dependent behavior. Specifically, the antisymmetric transfer function is selected as

$$H_1(\omega) = -H_2(\omega) = \frac{0.3\omega_0^2}{\omega^2 - \omega_0^2}, \tag{44}$$

where $\omega_0 = 4000\pi$ Hz. This transfer function is negative for $\omega < \omega_0$, positive for $\omega > \omega_0$, and exhibits a pole at $\omega = \omega_0$. The antisymmetry introduces a nonzero S_{21}, breaking Hermiticity and resulting in nonzero imaginary components in the dispersion relation, as shown in Fig. 5(a). Notably, the singularity at $\omega = \omega_0$ causes S_{21} to switch sign, leading to a sign reversal in the imaginary parts of the dispersion curves across the two branches. As shown in Fig. 5(b-c), the local resonance induces a band splitting in the real part of the dispersion relation, forming two distinct branches. The imaginary parts of the upper and lower branches exhibit opposite signs due to the change in S_{21}. While the conventional model captures the long-wavelength behavior of the first branch, the Willis effective model accurately reproduces both branches-demonstrating its effectiveness in modeling complex, frequency-dependent, non-Hermitian wave phenomena across the full frequency spectrum.

Non-Hermiticity alone does not necessarily lead to a complex spectrum. For instance, eigenvalues can remain real in the PT-unbroken phase and also in more general pseudo-Hermitian systems (Ashida et al., 2020). In our system, while verifying pseudo-Hermiticity is difficult, we observe purely real spectra under antisymmetric imaginary transfer functions. For transfer functions $H_1(\omega) = -H_2(\omega) = 0.3i$, Fig. 5(d) shows the imaginary part of S_{21}, whereas the real part is negligible and thus omitted. Although the presence of nonzero S_{21} breaks Hermiticity, the spectra in Fig. 5(e,f) remain entirely real. However, the real part of the dispersion relation becomes asymmetric with respect to the vertical axis due to the violation of reciprocity, as governed by Eq. (30). In this case, the wavenumbers for left-to-right and right-to-left wave propagation differ, directly reflecting the breakdown of the reciprocity condition. As expected, the conventional model can only capture the long-wavelength behavior, while the Willis effective model accurately reproduces the full-wave results across the entire frequency spectrum.

4. Non-Hermitian wave phenomena in the Willis effective beam

In this section, we demonstrate how our Willis effective framework enables a wide range of non-Hermitian wave phenomena in active beam systems. These effects arise from nonzero components of the effective polarizability tensor-particularly the off-diagonal

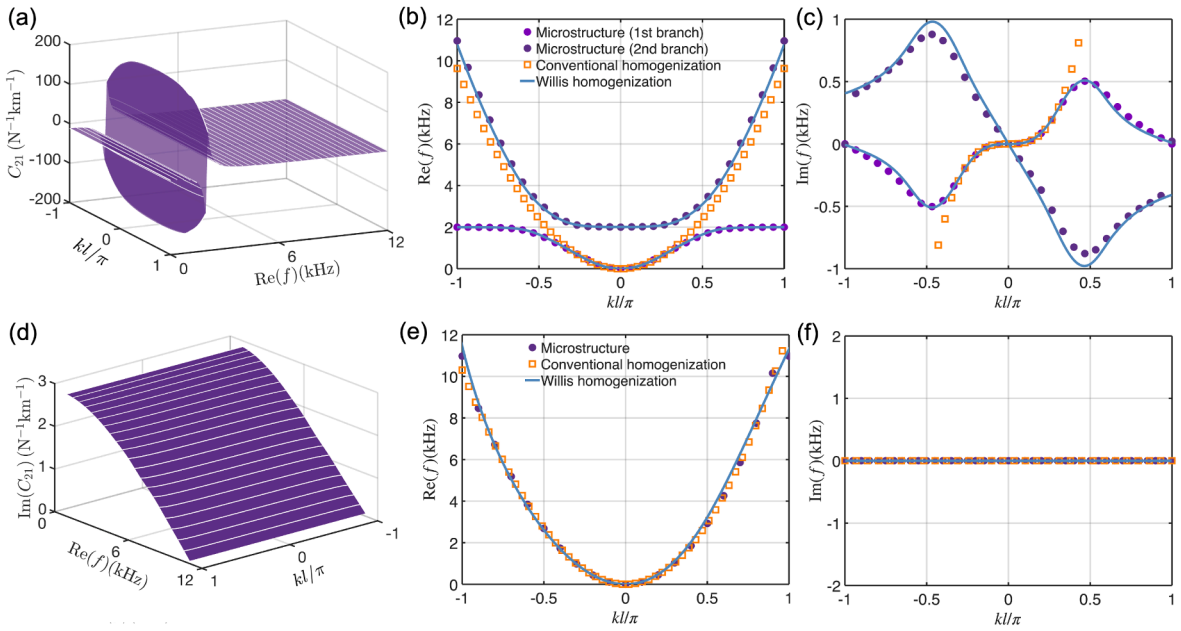

Fig. 5. Effective material properties and dispersion relations for locally resonant and antisymmetric imaginary transfer functions. (a-c) Locally resonant case: (a) S_{21} as a function of frequency and wavenumber, exhibiting a sign change due to the pole in the transfer function. (b) Real and (c) imaginary parts of the dispersion curves from microstructure simulation (dark and light purple dots for the first and second branches, respectively), conventional effective model (orange squares), and Willis effective model (blue solid line). The resonance introduces band splitting and a sign reversal in the imaginary dispersion. (d-f) Antisymmetric imaginary case: (d) Imaginary part of S_{21} as a function of frequency and wavenumber. (e) Real and (f) imaginary parts of the dispersion curves from microstructure simulation (purple dots), and predictions from conventional (orange squares) and Willis effective model (blue solid line). The non-Hermitian yet reciprocal nature yields real spectra with asymmetric dispersion.

S_{21}-which introduces directional couplings between bending moment and shear strain. We begin by examining how these couplings lead to low-frequency shear-enhanced flexural modes, a phenomenon absent in traditional beam models. We then reveal how the emergence of nonzero S_{21} breaks Maxwell-Betti reciprocity, resulting in non-Hermitian wave behavior such as nonreciprocal propagation and asymmetric dispersion. Finally, we extend our analysis to systems under OBC and establish a bulk-boundary correspondence between the winding number of the frequency spectrum and the emergence of skin modes. These results collectively highlight the power of the Willis homogenization framework to capture and engineer symmetry-broken, non-Hermitian effects in active beam systems.

4.1. *Flexural wave behavior under shear coupling in the Willis beam*

For antisymmetric transfer functions, $H_1(\omega) = -H_2(\omega)$, as discussed in Fig. 4(d-f), only the bending moment is sensed, while shear strain sources are applied, resulting in a nonzero β_{21} component in the polarizability tensor. From macroscopic perspective, this configuration enables directional coupling from bending moment to shear strain, giving rise to a nonzero K_{21} in the effective polarizability tensor. Notably, this coupling introduces shear deformation into the lowest dispersion branch-traditionally governed purely by bending deformation in conventional thin-beam theory-thereby generating a low-frequency flexural wave with shear contributions. To examine this effect, we begin by simplifying the dispersion relation in Eq. (34) as

$$\begin{pmatrix} S_{11} & 0 & 0 & -k\,i \\ S_{21} & 1/G_0 & -k\,i & 1 \\ 0 & k\,i & \omega^2\,\rho_0 & 0 \\ k\,i & 0 & 0 & J_0\,\omega^2 \end{pmatrix} \begin{pmatrix} M_{\text{eff}} \\ F_{\text{eff}} \\ w_{\text{eff}} \\ \psi_{\text{eff}} \end{pmatrix} = \begin{pmatrix} 0 \\ 0 \\ 0 \\ 0 \end{pmatrix} \tag{45}$$

where S_{11} and S_{21} are defined in Eq. (40). Eliminating M_{eff} and F_{eff} gives

$$\begin{bmatrix} -S_{11}\left(-\omega^2\rho_0 + G_0k^2\right) & -G_0k\left(S_{11}i - S_{21}k\right) \\ S_{11}G_0ki & -S_{11}G_0 + S_{11}J_0\omega^2 - S_{21}G_0ki - k^2 \end{bmatrix} \begin{bmatrix} w_{\text{eff}} \\ \psi_{\text{eff}} \end{bmatrix} = \begin{bmatrix} 0 \\ 0 \end{bmatrix} \tag{46}$$

Based on the Eq. (46) , the ratio of shear strain and rotation angle is obtained as

$$\frac{\gamma_{\text{eff}}}{\psi_{\text{eff}}} = \frac{ikw_{\text{eff}} - \psi_{\text{eff}}}{\psi_{\text{eff}}} = -\frac{(S_{11}i - S_{21}k)(-S_{11}\omega^2\rho_0 + 2S_{11}G_0k^2 + S_{21}G_0k^3i)}{S_{11}(-\omega^2\rho_0 + G_0k^2)(S_{11} + S_{21}ki)i} \tag{47}$$

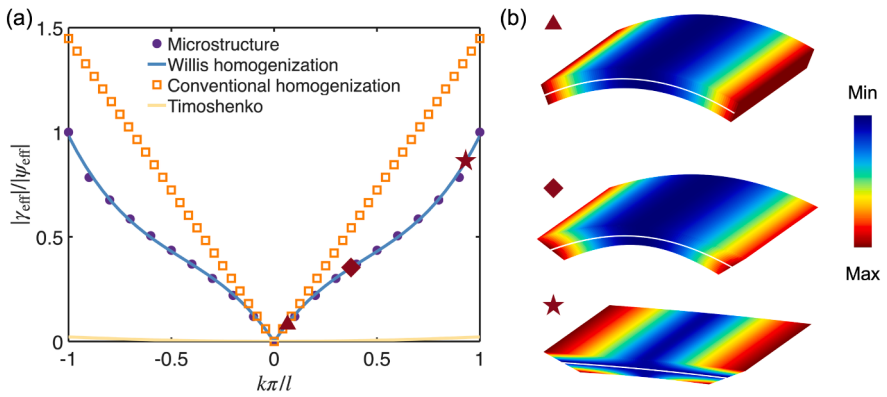

Fig. 6. Prediction of shear-to-rotation ratio and shear-enhanced flexural modes across wavenumbers. (a) Magnitude of the ratio $|\gamma_{\text{eff}}|/|\psi_{\text{eff}}|$ between effective shear strain and rotation angle, comparing results from microstructure simulation (purple dots), Willis effective model (blue solid line), conventional effective model (orange squares), and the classical Timoshenko beam model (yellow solid line), using antisymmetric transfer functions $H_1 = -H_2 = 1$. The ratio remains near zero in Timoshenko theory but increases significantly in the Willis effective model and microstructure as wavenumber increases. (b) Representative mode shapes from the Willis effective model at the triangle, diamond, and pentagram markers in (a), illustrating increasing shear deformation and cross-sectional distortion at higher wavenumbers.

Fig. 6(a) illustrate the change of magnitude of the ratio $|\gamma_{\text{eff}}|/|\psi_{\text{eff}}|$ in function of the wavenumber from the Willis effective model (blue solid line), the conventional effective model (orange squares), microstructure simulations (purple dots), and the Timoshenko theory (yellow solid line), which exhibit the unconventional coupling between the effective shear strain to the rotation angle. In the study, the antisymmetric transfer functions are selected as $H_1 = -H_2 = 1$. It is interesting to notice that the coupling magnitude increases significantly compared to the classical Timoshenko model, where this ratio remains near zero. Three representative mode shapes from the Willis effective model-corresponding to the triangle, diamond, and pentagram markers in Fig. 6(a)-are shown in Fig. 6(b). As the wavenumber increases, the neutral axis is no longer perpendicular to the boundaries, indicating enhanced shear deformation. Moreover, although the conventional model deviates from the microstructure dispersion in the short-wavelength regime, the Willis effective model accurately captures the behavior across the entire Brillouin zone. These results confirm that the Willis effective model supports low-frequency flexural waves coupled with shear deformation-an effect not realized in traditional thin beams. This shear-enhanced flexural mode offers new opportunities for impedance matching, wave control, and mode conversion in active mechanical systems.

4.2. Breakdown of the reciprocity theorem

In local media, reciprocity is equivalent to major symmetry (Nassar et al., 2020). In contrast, in nonlocal media, major symmetry alone does not guarantee reciprocity; instead, reciprocity emerges from the joint presence of major symmetry and time-reversal symmetry (Shokri and Rukhadze, 2019). In our system, the term S_{21} disrupts major symmetry, resulting in a violation of reciprocity. We now proceed to analyze reciprocity and its breakdown, beginning with the Green's function. In the frequency-wavenumber domain, the Green's function of the active Willis metabeam satisfies

$$\mathbf{H}\mathbf{G}_{\text{eff}}(\omega, k) = \mathbf{I}. \tag{48}$$

According to Eq. (30), the presence of S_{21} breaks the symmetry condition of $\mathbf{H}(\omega, k) \neq \mathbf{H}^T(\omega, -k)$,. Therefore, the Green's function $\mathbf{G}_{\text{eff}} = \mathbf{H}^{-1}$ no longer satisfies the symmetry condition $\mathbf{G}_{\text{eff}}(\omega, k) \neq \mathbf{G}^T_{\text{eff}}(\omega, -k)$ which translates to

$$\mathbf{G}_{\text{eff}}(\omega, x - x') \neq \mathbf{G}^T_{\text{eff}}(\omega, x' - x) \tag{49}$$

in the spatial domain. To assess the reciprocity condition, we perform two load-response numerical experiments. In the first scenario, the external load is $\mathbf{Q}^1_{\text{ext}}(\omega, x)$ applied, yielding the response $\mathbf{u}^1_{\text{eff}}(\omega, x)$. In the second scenario, the applied load is $\mathbf{Q}^2_{\text{ext}}(\omega, x)$ with the corresponding response $\mathbf{u}^2_{\text{eff}}(\omega, x)$. The reciprocity condition is expressed as (Nassar et al., 2020)

$$\int_L (\mathbf{u}^2_{\text{eff}})^T(\omega, x)\mathbf{Q}^1_{\text{ext}}(\omega, x)dx = \int_L (\mathbf{u}^1_{\text{eff}})^T(\omega, x)\mathbf{Q}^2_{\text{ext}}(\omega, x)dx. \tag{50}$$

Using the response relation $\mathbf{u}_{\text{eff}}(\omega, x) = \int_L \mathbf{G}_{\text{eff}}(\omega, x - x')\mathbf{Q}_{\text{ext}}(x')dx'$ and taking the transpose and interchanging x and x' on the right-hand side, the reciprocity condition can be rewritten as

$$\int_L \int_L (\mathbf{Q}^2_{\text{ext}})^T(\omega, x')\mathbf{G}^T_{\text{eff}}(\omega, x - x')\mathbf{Q}^1_{\text{ext}}(\omega, x)\, dx dx' = \int_L \int_L (\mathbf{Q}^2_{\text{ext}})^T(\omega, x')\mathbf{G}_{\text{eff}}(\omega, x' - x)\mathbf{Q}^1_{\text{ext}}(\omega, x)\, dx dx'. \tag{51}$$

Therefore, Eq. (51) shows that the reciprocity condition in Eq. (50) is equivalent to the symmetry condition of the Green's function $\mathbf{G}_{\text{eff}}(\omega, x - x') = \mathbf{G}^T_{\text{eff}}(\omega, x' - x)$. In our study, the presence of S_{21} breaks this symmetry condition, leading to the inequality in Eq. (49). As a result, the equality in Eq. (51) is violated, thereby breaking the reciprocity theorem in Eq. (50).

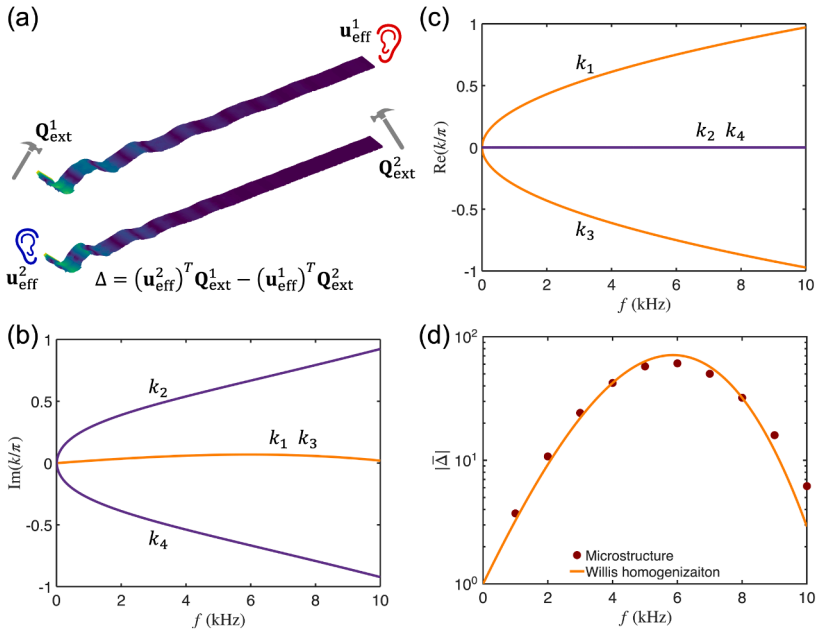

Fig. 7. Nonreciprocal wave propagation in Willis media. (a) Schematic of the nonreciprocity test: A shear force is applied at either end of the beam (input positions), and the displacement is measured at the opposite end (output positions). Nonreciprocity is quantified by the difference Δ. (b) Real part and (c) imaginary part of the wavenumber-frequency (k-ω) dispersion relations from the Willis effective model, showing four complex wavenumber branches k_1-k_4. (d) Magnitude of the normalized nonreciprocity parameter $|\bar{\Delta}|$ versus frequency, comparing microstructure simulation (red dots) and Willis effective model (orange line).

We now numerically verify the breaking of the reciprocity theorem using COMSOL simulations with constant antisymmetric transfer functions $H_1(\omega) = -H_2(\omega) = 0.3$. The length of beam with microstructures is L and two perfect matched layers are attached on both sides. Two numerical tests are performed: in the first case, a unit shear force $\mathbf{Q}^1_{\text{ext}}(x) = [0,0,0,1]^T\delta(x)$ is applied at $x = 0$, and the resulting displacement w_1 is measured at $x = L$, as shown in Fig. 7(a). In the second case, a unit shear force $\mathbf{Q}^2_{\text{ext}}(x) = [0,0,0,1]^T\delta(x-L)$ is applied at $x = L$, and the displacement w_2 is measured at $x = -L$, as illustrated in Fig. 7(a). The difference between the left-hand side and right-hand side of Eq. (50) is given by

$$\Delta = (\mathbf{u}^2_{\text{eff}})^T\mathbf{Q}^1_{\text{ext}} - (\mathbf{u}^1_{\text{eff}})^T\mathbf{Q}^2_{\text{ext}} = w_2 - w_1 \tag{52}$$

The measured magnitude of Δ, normalized by $|w_2|$, as a function of frequency is shown in Fig. 7(a). Since $|\Delta|/|w_1|$ is nonzero, Δ does not vanish, confirming the violation of the reciprocity theorem.

We now proceed to solve the Green's function for an infinite beam using an asymptotic approach. In the asymptotic limit, the Green's function depends solely on the k-ω dispersion relation. Therefore, we begin by computing the dispersion relations, shown in Fig. 7(a-b), using the material and geometric parameters provided in Appendix D and antisymmetric transfer functions $H_1(\omega) = -H_2(\omega) = 0.3$. For a given frequency, four complex wavenumbers arise. Among these, two wavenumbers (k_2, k_4) are purely imaginary, as indicated by the purple lines in Fig. 7(a-b), while the other two (k_1, k_3) possess symmetric real parts and degenerate imaginary parts, as shown by the orange lines. When L is large, an asymptotic approximation yields

$$\Delta = G^{11}_{\text{eff}}(\omega, L) - G^{11}_{\text{eff}}(\omega, -L) \sim \frac{1}{\sqrt{2\pi}} G^{11}_{\text{eff}}(\omega, k_1) e^{ik_1 L}. \tag{53}$$

A detailed derivation is provided in Appendix A.

To verify the nonreciprocity, we perform finite element simulations on a microstructured beam composed of 20 unit cells, with perfectly matched layers attached to both ends, as shown in Fig. 7(c). In these simulations, a shear load is applied separately on the left and right ends of the beam. The response of the metabeam exhibits attenuation under left-side loading and amplification under right-side loading, clearly indicating directional asymmetry. The frequency dependence of the nonreciprocity parameter $\bar{\Delta}$, defined in Eq. (52), is presented in Fig. 7(d). The red dots represent results from the microstructure simulations, while the orange line corresponds to the theoretical prediction from Eq. (52) combined with Eq. (A.22). As shown in Fig. 7(d), $\bar{\Delta}$ approaches 1 as the frequency tends toward 0 Hz, and exceeds 1 when the frequency is nonzero, confirming the breakdown of reciprocity. With increasing frequency, $\bar{\Delta}$ rises rapidly, reaching a maximum value of approximately 170 at 6 kHz, and then gradually decreases for higher frequencies. These results demonstrate giant nonreciprocity and reveal the potential for achieving giant nonreciprocity in the proposed system.

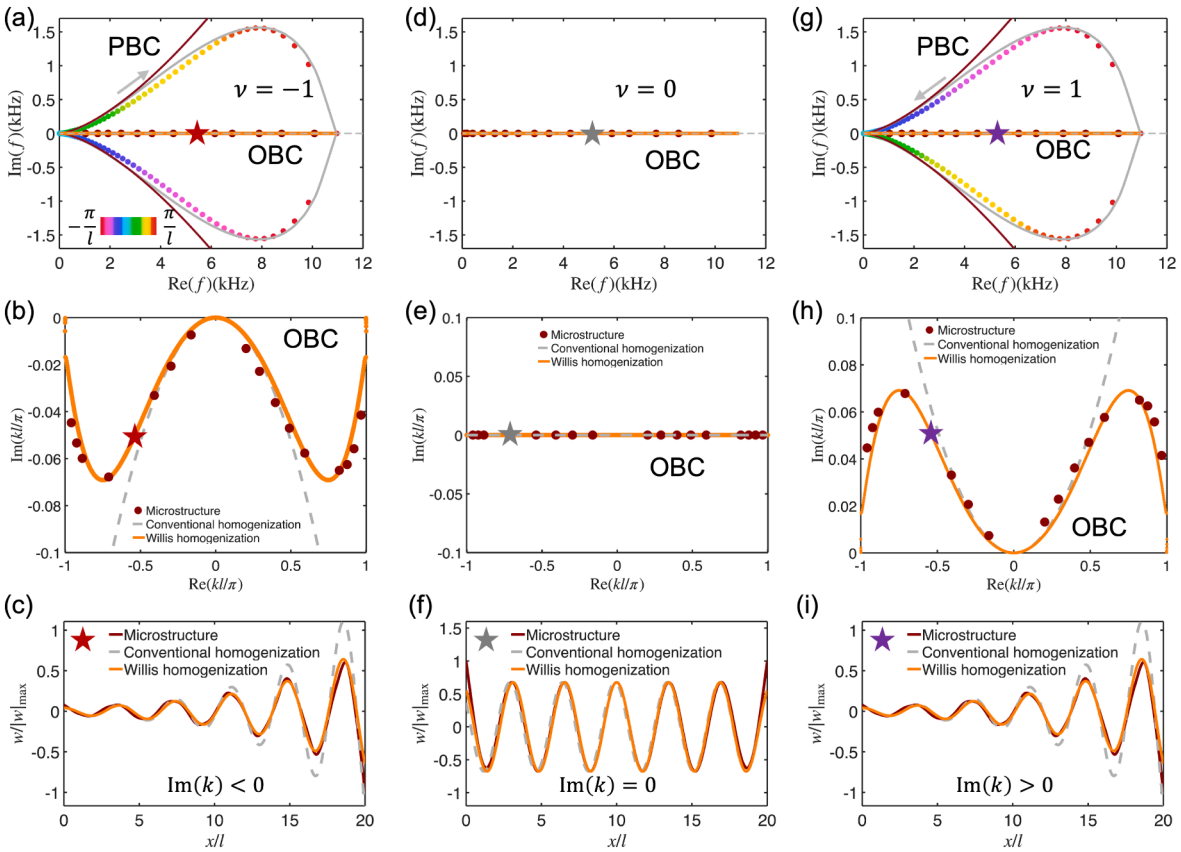

Fig. 8. PBC and OBC frequency spectra, GBZ, and skin modes for constant antisymmetric transfer functions. (a-c) Case with $H_1 = -H_2 = 0.3$: (a) Frequency spectra of the flexural branch under PBC from the Willis effective model (gray solid lines), conventional effective model (red solid lines), and microstructure simulations (color-gradient dots). The corresponding OBC spectra are shown as orange lines (Willis effective model) and red dots (microstructure). The winding number of PBC spectral is $\nu = -1$. (b) GBZ extracted from the OBC spectra in (a) for the Willis effective model (orange solid lines), conventional model (gray dashed lines), and microstructure (red dots). (c) Eigenmodes at the pentagram frequencies in (a), showing directional localization consistent with the sign of $\mathrm{Im}(k)$, computed from the Willis effective model (orange solid lines), conventional model (blue dashed lines), and microstructure simulation (purple solid lines). (d-f) Corresponding results for the Hermitian case $H_1 = -H_2 = 0$ with winding number $\nu = 0$, showing extended modes and undeformed GBZ. The frequency spectra under PBC are omitted, as they coincide with the OBC spectra. (g-i) Results for $H_1 = -H_2 = -0.3$ with winding number $\nu = 1$, exhibiting reversed skin mode localization and GBZ deformation opposite to the case in (a-c).

4.3. Non-Bloch band theory and bulk-boundary correspondence

In non-Hermitian systems, conventional Bloch band theory fails under OBC, necessitating the use of non-Bloch band theory and the GBZ to correctly describe wave behavior. However, for complex microstructures, directly applying this theory is often infeasible due to analytical inaccessibility. The non-Hermitia Willis effective medium offers a powerful alternative: it captures nonlocal and symmetry-breaking effects while maintaining analytical tractability. Under periodic boundary conditions (PBCs), the Willis effective model yields closed spectral loops in the complex frequency plane, enabling the definition of topological invariants such as the spectral winding number-something the conventional effective medium fails to provide due to its open spectral curves. This allows the Willis effective model to support a robust bulk-boundary correspondence, in which the winding number predicts the existence and localization direction of skin modes under OBCs. In this section, we employ the non-Hermitia Willis medium to explore non-Bloch band theory, compute spectral winding numbers and demonstrate their correspondence with skin-mode localization, providing a comprehensive framework for understanding topological wave phenomena in active elastic systems.

4.3.1. Non-Bloch band theory

First, we develop the non-Bloch band theory by solving the BVP for a finite beam with specified boundary conditions using asymptotic analysis. For the non-Hermitian medium, the dispersion relation in Eq. (36) yields four wavenumber roots for a given frequency, denoted as k_n for $n = 1, 2, 3, 4$. The general solution for the transverse displacement of the non-Hermitia Willis metabeam

is given by

$$w_{\text{eff}}(x) = \sum_{n=1}^{4} A_n e^{ik_n x} \tag{54}$$

where A_n are the corresponding coefficients. The rotational angle is expressed as

$$\psi_{\text{eff}}(x) = \sum_{n=1}^{4} A_n N_\psi^n e^{ik_n x} \tag{55}$$

where N_ψ^n is the amplitude ratio obtained by solving homogenious equation $\mathbf{H}\mathbf{u}_{\text{eff}} = \mathbf{0}$ with the dispersion relation in Eq. (36). Now, we consider the BVP using fixed boundary conditions as an example:

$$w_{\text{eff}}(0) = 0, \quad \psi_{\text{eff}}(0) = 0, \quad w_{\text{eff}}(L) = 0, \quad \psi_{\text{eff}}(L) = 0. \tag{56}$$

where L is the length of the finite metabeam. Substituting the wave solutions into these boundary conditions, we obtain the following equations

$$\begin{pmatrix} 1 & 1 & 1 & 1 \\ N_\psi^1 & N_\psi^2 & N_\psi^3 & N_\psi^4 \\ e^{ik_1 L} & e^{ik_2 L} & e^{ik_3 L} & e^{ik_4 L} \\ N_\psi^1 e^{ik_1 L} & N_\psi^2 e^{ik_2 L} & N_\psi^3 e^{ik_3 L} & N_\psi^4 e^{ik_4 L} \end{pmatrix} \begin{pmatrix} A_1 \\ A_2 \\ A_3 \\ A_4 \end{pmatrix} = \begin{pmatrix} 0 \\ 0 \\ 0 \\ 0 \end{pmatrix} \tag{57}$$

Setting the determinant of the coefficient matrix to zero yields the frequency spectrum under fixed boundary conditions

$$\begin{vmatrix} 1 & 1 & 1 & 1 \\ N_\psi^1 & N_\psi^2 & N_\psi^3 & N_\psi^4 \\ e^{ik_1 L} & e^{ik_2 L} & e^{ik_3 L} & e^{ik_4 L} \\ N_\psi^1 e^{ik_1 L} & N_\psi^2 e^{ik_2 L} & N_\psi^3 e^{ik_3 L} & N_\psi^4 e^{ik_4 L} \end{vmatrix} = 0 \tag{58}$$

Next, we derive the GBZ by extending the method developed for lattice systems (Yokomizo and Murakami, 2019). The solution of Eq. (58) simplifies for large L, forming the corresponding continuum spectrum. Expanding the determinant in Eq. (58), we obtain

$$\begin{aligned} &F_1\left(\vec{k},\omega\right)e^{i(k_1+k_2)L} + F_2\left(\vec{k},\omega\right)e^{i(k_1+k_3)L} + F_3\left(\vec{k},\omega\right)e^{i(k_1+k_4)L} \\ &+ F_4\left(\vec{k},\omega\right)e^{i(k_2+k_3)L} + F_5\left(\vec{k},\omega\right)e^{i(k_2+k_4)L} + F_6\left(\vec{k},\omega\right)e^{i(k_3+k_4)L} = 0 \end{aligned} \tag{59}$$

Here, $\vec{k} = [k_1, k_2, k_3, k_4]$, and $F_i(\vec{k},\omega)$ $(i = 1, 2, \ldots, 6)$ are coefficients that depend on both frequency and wavenumbers, obtained by expanding the determinant in Eq. (58). We now analyze the asymptotic behavior of the solutions of Eq. (59) for large L, where the wavenumbers are ordered as $\text{Im}(k_1) < \text{Im}(k_2) < \text{Im}(k_3) < \text{Im}(k_4)$ for convenience.

If $\text{Im}(k_2) \neq \text{Im}(k_3)$, only one leading term proportional to $F_6(\vec{k},\omega)e^{i(k_3+k_4)L}$ remains in Eq. (59) in the limit of large L. This leads to

$$F_6\left(\vec{k},\omega\right) = 0 \tag{60}$$

which does not depend on L and does not allow for a continuous frequency spectrum.

On the other hand, when $\text{Im}(k_2) = \text{Im}(k_3)$, two leading terms proportional to $e^{i(k_2+k_4)L}$ and $e^{i(k_3+k_4)L}$ remain, allowing Eq. (59) to be rewritten as

$$e^{i(k_2-k_3)L} = -\frac{F_6\left(\vec{k},\omega\right)}{F_5\left(\vec{k},\omega\right)} \tag{61}$$

In such a case, we can expect that the difference between $\text{Re}\left(k_2\right)$ and $\text{Re}\left(k_3\right)$ can be changed almost continuously for a large L, producing continuum frequency spectrum. Finally, in the asymptotic limit $L \to \infty$, the boundary value problem of the nonlocal non-Hermitian metabeam reduces to two algebraic equations:

$$\begin{aligned} &|\mathbf{H}(\omega,k)| = 0, \\ &\text{Im}\left(k_2(\omega)\right) = \text{Im}\left(k_3(\omega)\right). \end{aligned} \tag{62}$$

For a given complex frequency ω, the first equation in Eq. (62) yields four frequency-dependent wavenumbers $k_1(\omega)$, $k_2(\omega)$, $k_3(\omega)$, and $k_4(\omega)$, ordered as $\text{Im}(k_1) < \text{Im}(k_2) < \text{Im}(k_3) < \text{Im}(k_4)$. Among these, the second and third wavenumbers satisfy the second equation in Eq. (62). The first equation is complex and can be decomposed into two real equations, yielding a total of three real equations involving four independent real variables: $\text{Re}(\omega)$, $\text{Im}(\omega)$, $\text{Re}(k)$, and $\text{Im}(k)$. As a result, the solutions $(\text{Re}(\omega), \text{Im}(\omega), \text{Re}(k), \text{Im}(k))$ form continuous curves in the four-dimensional space. When projected onto the complex ω-plane, these solutions appear as continuous curves, ensuring that the frequency spectrum remains continuous. Similarly, their projection onto the complex k-plane forms continuous curves, known as the GBZ. The GBZ extends the conventional Brillouin zone-defined as the real interval from $-\pi/l$ to π/l in

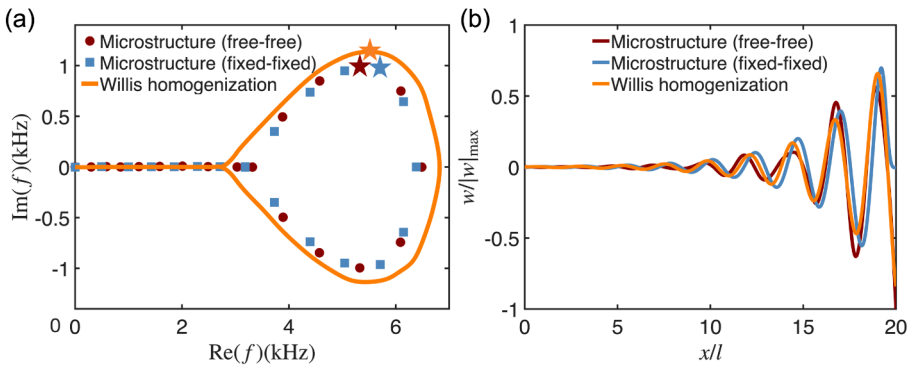

Fig. 9. Comparison of open-boundary spectra and modes for different boundary conditions. (a) Complex frequency spectrum of the microstructured beam with constant transfer functions $H_1(\omega) = -H_2(\omega) = 1$ for free-free (red circles) and fixed-fixed (blue squares) boundaries, compared with the OBC spectrum predicted by the Willis homogenization (orange curve). (b) Normalized transverse displacement profiles of the eigenmodes, where the red, blue, and orange curves correspond to the red, blue, and orange stars in (a), respectively.

Hermitian systems-into curves in the complex plane, and plays a fundamental role in capturing the spectral and localization properties unique to non-Hermitian physics. It is crucial for reconstructing the bulk-boundary correspondence of the Chern number and topological edge modes, as well as for computing the Green's function to determine system responses, such as stress or strain, under external excitations in engineering applications. To solve complex Eq. (62) numerically is challenging since many numerical methods are designed for real-valued equations. To address this, for a given variable such as Re(ω), Eq. (62) can be reformulated as three real equations involving three real independent unknowns. Numerical techniques such as Newton's method, iterative solvers, or gradient-based optimization can then be applied. Here, we use "fsolve" function in MATLAB. By sweeping Re(ω) over the desired range, continuous frequency spectra and GBZ can be obtained.

In deriving Eq. (62), fixed boundary conditions are used. However, in the asymptotic limit, the frequency spectrum equation in Eq. (62) remains independent of the specific boundary conditions. For other boundary conditions, such as free, simply supported, or mixed conditions, the coefficients $F_i(\vec{k},\omega)$ $(i = 1, 2, \ldots, 6)$ will change, but the spectrum condition $\mathrm{Im}\big(k_2(\omega)\big) = \mathrm{Im}\big(k_3(\omega)\big)$ remains unaffected. Therefore, the frequency spectrum can be determined by solving Eq. (59) regardless of the boundary conditions. In other words, the frequency spectrum under OBC is independent of the specific type of boundary conditions. To corroborate this prediction, we compare in Fig. 9 the complex spectra and mode shapes of the microstructured beam with fixed-fixed and free-free boundaries for constant transfer functions $H_1(\omega) = -H_2(\omega) = 1$. The discrete eigenfrequencies for both boundary conditions nearly collapse onto the same spectral loop and follow closely the asymptotic OBC spectrum obtained from the Willis homogenization, confirming that the bulk spectrum is insensitive to the choice of boundary conditions. The slight discrepancy between the microstructure and Willis homogenization results arises because the metabeam used in the simulations is not sufficiently long; increasing its length makes the two results converge more closely. The corresponding eigenmodes show visible differences only in the immediate vicinity of the right boundary, where the local shape is constrained by the imposed end condition. Away from the boundary, however, the envelopes of the two modes almost coincide and exhibit the same exponential decay rate, in agreement with the prediction from Eq. (62). This comparison demonstrates that boundary conditions only affect a narrow boundary layer, while the OBC spectrum and decaying behavior remain independent of the specific type of boundary conditions.

We now turn to study frequency spectra, GBZ, and mode shapes numerically. The geometric and material parameters used in this subsection are listed in Appendix D, and the microstructure simulations are performed on a finite beam of length $20l$. For the constant transfer functions $H_1(\omega) = -H_2(\omega) = \pm 0.3$, Fig. 8(a) presents the frequency spectra under both PBC and OBC. The antisymmetric transfer function introduces directional coupling, breaking Hermiticity and causing the PBC spectra from the microstructure (gradient-colored dots) to form a closed loop in the complex frequency plane. The conventional model, using a constant S_{21}, captures only part of this loop, whereas the Willis effective model, which accounts for frequency- and wavenumber-dependent S_{21}, successfully reconstructs the full loop-highlighting its superior predictive capability. Despite the non-Hermiticity, the OBC spectra remain entirely real, likely reflecting a *PT*-unbroken phase. As shown in Fig. 8(a), the OBC spectrum from the microstructure (red dots) ranges from 0 to approximately 11.5 kHz and matches closely with the prediction from the Willis effective model (orange solid lines), whereas the conventional model (gray dashed lines) overestimates the upper frequency bound. The corresponding GBZ, which represent the wavenumber distributions of OBC spectra, are plotted in Fig. 8(b). The wavenumbers have negative imaginary parts, indicating right-localized skin modes, which is confirmed by the mode shapes at the pentagram-marked frequency in Fig. 8(c). The Willis effective model again closely matches the microstructure simulation, whereas the conventional model fails to predict the correct localization strength. For the Hermitian case $H_1(\omega) = -H_2(\omega) = 0$, the PBC and OBC spectra are identical, and thus the PBC spectra are omitted in Fig. 8(d). As shown in Fig. 8(e), the OBC spectrum remains purely real, and both the Willis effective model and microstructure yield nearly identical results. Although the conventional model still fails to predict the upper bound, it reproduces the mode shapes reasonably well, as shown in Fig. 8(f). Finally, Fig. 8(g-i) shows the results for $H_1(\omega) = -H_2(\omega) = 0.3$. Compared to the case with $H_1(\omega) = -H_2(\omega) = -0.3$, the direction of the PBC frequency loop reverses, the GBZ flips sign, and the localization of skin modes

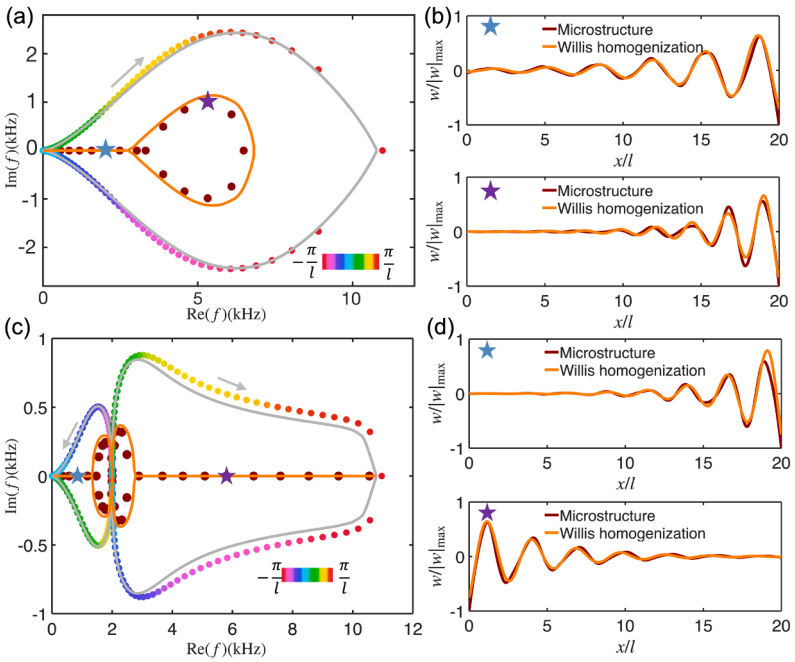

Fig. 10. PBC and OBC frequency spectra, GBZs, and skin modes for large constant and locally resonant antisymmetric transfer functions. (a) Frequency spectrum of the flexural mode under PBC (gradient-colored dots) and fixed boundary conditions (OBC, red dots) from COMSOL simulations, for constant transfer functions $H_1(\omega) = -H_2(\omega) = 1$. The gray solid loop is computed from the dispersion relation in Eq. (36) for the Willis effective model under PBC, while the orange solid line corresponds to the OBC spectrum derived from the boundary value problem in Eq. (62). (b) Eigenmodes at the pentagram frequencies in (a), calculated from the Willis effective model (orange solid lines) and COMSOL simulations (purple solid lines), demonstrating skin effect localization. (c) Frequency spectrum under the same boundary conditions and representations as in (a), but using frequency-dependent resonant transfer functions defined in Eq. (44). The presence of two spectral loops reflects the frequency-dependent nature of the active scatterers. (d) Corresponding eigenmodes at the pentagram frequencies in (c), showing excellent agreement between the Willis effective model and the microstructure simulations.

switches from right to left. This inversion stems from the change in the direction of the directional coupling and the sign flip of S_{21}, while the magnitudes of the relevant quantities remain unchanged.

As the transfer function strength increases to $H_1(\omega) = -H_2(\omega) = 1$, the PBC frequency spectra-depicted by gray solid lines for the Willis effective model and gradient-colored dots for the microstructure-retain their closed-loop structure but develop larger imaginary components, as shown in Fig. 10(a). Under OBC, the microstructure spectrum (red dots) remains real at low frequencies but transitions into complex-conjugate pairs at higher frequencies, signaling the presence of an exceptional point. This transition is accurately captured by the Willis effective model (orange lines), with slight discrepancies near the spectral edges attributable to finite beam length effects, which diminish as the length increases. The eigenmodes at the two pentagram-marked frequencies in Fig. 10(a) are shown in Fig. 10(b), both exhibiting right-side localization. For the resonant transfer functions defined in Eq. (44), the PBC spectrum-again shown as gray lines and gradient-colored dots-splits into two distinct loops, indicating the emergence of multiple spectral branches due to local resonance. The corresponding OBC spectrum in Fig. 10(c) features complex-conjugate eigenvalues near 2 kHz, and purely real values below 1.5 kHz and above 2.7 kHz. The associated mode shapes at the two pentagram markers are shown in Fig. 10(d), now exhibiting opposite localization directions. The Willis effective model continues to match the microstructure results closely, with residual deviations primarily resulting from the finite beam length.

4.3.2. Bulk-boundary correspondence

Before turning to the explicit winding-number formulation, we briefly clarify how different non-Hermitian mechanisms enter the effective operator and give rise to skin modes. At the level of the effective operator, the three mechanisms mentioned-asymmetric density, asymmetric elasticity, and asymmetric Willis coupling-affect the complex spectrum and the emergence of skin modes in the same structural way: they all introduce non-reciprocal couplings that break Hermiticity in the bulk operator. Meanwhile, the breakdown of these symmetries in the constitutive relations originates, from a microscopic perspective, from nonreciprocal couplings. Such nonreciprocal couplings break parity symmetry in one-dimensional systems, leading to $\omega(k) \neq \omega(-k)$. This $k \to -k$ asymmetry serves as a necessary condition for the PBC spectrum to form complex eigenvalue loops with nonzero point-gap winding; otherwise, the winding is trivial and the skin effect is suppressed. Any of these mechanisms can therefore serve as a necessary condition for non-Hermitian behavior and can, in principle, support skin modes. However, the existence of skin modes is not set by the microscopic origin of non-Hermiticity, but by the bulk-boundary correspondence encoded in the complex spectrum: skin modes appear if and only if the complex eigenvalue loops under PBC exhibit a nonzero winding number, as established in Okuma et al. (2020), Zhang

et al. (2020). In this sense, density asymmetry, elastic asymmetry, and Willis asymmetry are different microscopic routes to the same effective condition: a non-Hermitian operator with a spectrum of nontrivial winding. In the present metabeam, the only non-Hermitian contribution comes from the asymmetric off-diagonal entries of the compliance matrix, i.e., $S_{12} \neq S_{21}$, while the effective density and Willis blocks remain zero or symmetric. Thus, the skin modes observed in Figs. 8 and 10 are driven solely by this asymmetric elastic coupling in $\mathbf{S}$, and their existence and boundary accumulation are determined by the nonzero spectral winding number of the PBC spectrum. In what follows, we make this bulk-boundary correspondence explicit using the winding number of the PBC spectrum.

The non-Bloch band theory provides a complete description of the frequency spectrum, GBZ, and mode shapes. However, it is numerically demanding due to the need to solve complex-valued equations. In contrast, the frequency spectrum under PBC is easier to compute, and partial information about OBC spectra and mode localization can be inferred from the bulk-boundary correspondence. Notably, the Willis effective model accurately captures the full PBC spectrum, whereas the conventional effective model fails to do so. This makes the Willis effective model a powerful and accessible tool for establishing the bulk-boundary correspondence and predicting skin mode behavior. In our system, multiple eigenfrequencies $\omega_\alpha(k)$ may exist for a given wavenumber under PBC. In non-Hermitian systems, these frequencies generally form closed loops in the complex plane, which are topologically protected as long as a base point ω_b remains enclosed. In one-dimensional systems, such loops are quantitatively characterized by the winding number of the spectrum (Ashida et al., 2020), given by

$$\nu(\omega_b) = \sum_\alpha \int_{-\pi/l}^{\pi/l} \frac{\mathrm{d}k}{2\pi} \frac{d}{dk} \arg\left[\omega_\alpha(k) - \omega_b\right]. \tag{63}$$

For antisymmetric transfer functions $H_1(\omega) = -H_2(\omega)$, the complex frequency spectrum under PBC is shown in Fig. 8(a) for $H_1(\omega) = 0.3$, Fig. 8(d) for $H_1(\omega) = 0$, and Fig. 8(g) for $H_1(\omega) = -0.3$. In the left panel, the spectral loop rotates clockwise as k varies from $-\pi/l$ to π/l, yielding a winding number $\nu(\omega_b) = -1$ for any base frequency ω_b enclosed by the loop. In the middle panel, the frequency spectrum collapses to a line, indicating a winding number of zero for any ω_b. In the right panel, the spectral loop rotates counterclockwise as k varies from $-\pi/l$ to π/l, resulting in a winding number $\nu(\omega_b) = 1$ for any base frequency ω_b inside the loop. For antisymmetric transfer functions $H_1(\omega) = -H_2(\omega) = 1$, the complex frequency spectrum under PBC is shown in Fig. 10(a). The spectrum forms a clockwise loop, indicating a winding number $\nu(\omega_b) = -1$ for any base frequency ω_b enclosed by the loop. When the antisymmetric transfer function follows the resonant form in Eq. (44), the complex frequency spectrum under PBC is shown in Fig. 10(c). In this case, the spectrum consists of a counterclockwise loop on the left and a clockwise loop on the right. Consequently, the winding number $\nu(\omega_b)$ is 1 for any base frequency ω_b inside the left loop and -1 for any base frequency inside the right loop.

The bulk-boundary correspondence in non-Hermitian systems has two key components, both efficiently captured by the Willis effective model. The first one is the relationship between the frequency spectra under PBC and OBC. In non-Hermitian systems, the OBC spectrum is always enclosed by the PBC spectrum. The Willis effective model accurately reproduces both, even under strong or resonant transfer functions. For instance, in Fig. 8(a,c), with small transfer functions, the OBC spectrum remains real and is tightly enclosed by the PBC spectral loop. As the transfer function magnitude increases, the OBC spectrum becomes complex while still enclosed by the PBC spectrum, as seen in Fig. 10(a). In the resonant case (Fig. 10(c)), the PBC spectrum splits into two distinct loops, each surrounding portions of the OBC spectrum. These behaviors are faithfully captured by the Willis effective model, in contrast to the conventional model, which cannot reconstruct the full PBC spectrum and thus fails to reflect the bulk-boundary correspondence structure. The second component of bulk-boundary correspondence connects the sign of the winding number, calculated from the PBC spectrum, to the localization direction of skin modes under OBC. The Willis effective model provides a continuous, nonlocal medium where this relation becomes apparent. A negative winding number implies right-edge localization (Fig. 8(c)); zero implies extended modes (Fig. 8(f)); and a positive value leads to left-edge localization (Fig. 8(i)). These results hold consistently across different transfer functions, as further demonstrated in Fig. 10(b, d). Moreover, instead of computing the full GBZ, which is typically complex and computationally demanding, the sign of the winding number from the PBC spectrum suffices to predict skin mode localization. The Willis effective model thus offers both physical clarity and computational simplicity, serving as a powerful tool for analyzing non-Hermitian topological effects in active media.

5. Conclusion

This work presents a comprehensive Willis homogenization framework tailored for metabeams comprising periodically arranged active or self-sensing scatterers. These scatterers are physically implemented using piezoelectric sensor-actuator pairs integrated with digital control circuits that encode programmable transfer functions. Leveraging a source-driven homogenization approach, the framework rigorously captures the full frequency- and wavenumber-dependent behavior of wave propagation across the system. The resulting Willis effective model accurately reproduces both real and imaginary components of the dispersion relations throughout the entire Brillouin zone, as validated by detailed numerical simulations based on the underlying microstructure. This demonstrates the model's ability to describe complex, high-frequency, and short-wavelength dynamics-well beyond the scope of traditional homogenization methods. Furthermore, the framework enables the prediction and analysis of a range of non-Hermitian wave phenomena, including low-frequency shear-enhanced flexural modes, directional amplification, and the presence of non-Hermitian skin modes under OBC. Through asymptotic analysis, we develop a non-Bloch band theory and establish a bulk-boundary correspondence that directly links the spectral winding number under periodic boundary conditions to the spatial localization of modes within the effective Willis model. This provides a physically grounded and analytically tractable approach for exploring non-Hermitian topological mechanics. Collectively, the results establish a unified and versatile methodology for modeling, realizing, and controlling wave behavior

in active elastic media with arbitrary symmetry-breaking configurations. The proposed framework lays a robust foundation for future advancements in programmable metamaterials, topological wave control, and wave-based functional devices.

CRediT authorship contribution statement

Shaoyun Wang: Writing – review & editing, Writing – original draft, Visualization, Validation, Software, Methodology, Investigation, Formal analysis, Conceptualization; **Honghua Qian:** Writing – review & editing, Writing – original draft, Visualization, Validation, Investigation, Formal analysis; **Jiaji Chen:** Writing – review & editing, Visualization, Software, Methodology; **Nan Shao:** Visualization, Validation, Methodology, Formal analysis, Conceptualization; **Wen Cheng:** Visualization, Validation, Methodology; **Heng Jiang:** Writing – review & editing, Methodology, Conceptualization; **Rui Zhu:** Writing – review & editing, Methodology, Investigation; **Guoliang Huang:** Writing – review & editing, Writing – original draft, Validation, Supervision, Methodology, Conceptualization.

Data availability

No data was used for the research described in the article.

Declaration of competing interest

The authors declare no known competing financial interests or personal relationships that could have influenced the work reported in this paper.

Acknowledgments

G. L. Huang acknowledges the support from the Peking University start-up Grant and the National Natural Science Foundation of China (Grant No. W2531003). The authors thank Dr. Zhanyu Li for their valuable discussions.

Appendix A. Green's function

A.1. Displacement response in Timoshenko beam

In the frequency-space domain, the governing equation in Eq. (4) can be written as

$$\boldsymbol{\zeta}(\omega, -i\partial_x)\,\mathbf{u} = \mathbf{Q}. \tag{A.1}$$

By eliminating the internal variables M, F, and ψ from Eq. (A.1), we obtain the reduced governing equation for transverse displacement w:

$$\begin{aligned} &D_0\frac{\partial^4 w}{\partial x^4} + J_0\omega^2\left(1+\frac{D_0P_0}{G_0J_0}\right)\frac{\partial^2 w}{\partial x^2} + \left(\frac{J_0\rho_0\omega^4}{G_0} - \rho_0\omega^2\right)w \\ &\quad = -\frac{\partial q}{\partial x} + \left(1-\frac{J_0}{G_0}\omega^2\right)f - \frac{D_0}{G_0}\frac{\partial^2 f}{\partial x^2} + D_0\frac{\partial^2 p}{\partial x^2} + D_0\frac{\partial^3 s}{\partial x^3} + J_0\omega^2\frac{\partial s}{\partial x}, \end{aligned} \tag{A.2}$$

where f, p, q, and s are external force sources.

When only a shear force is applied, i.e., $f = \delta(x)$, Eq. (A.2) reduces in the reciprocal space to

$$w(\omega, k) = \frac{1}{D_0}\frac{1-\frac{J_0}{G_0}\omega^2+\frac{D_0}{G_0}k^2}{(k^2+a^2)(k^2+b^2)}, \tag{A.3}$$

where $a = ik_1$, $b = k_2$, and k_1, k_2 are positive real numbers satisfying the dispersion relation $\det[\boldsymbol{\zeta}(\omega, k)] = 0$ for a given frequency ω.

The corresponding inverse Fourier transform yields the spatial response:

$$w(\omega, x) = \frac{1}{2D_0}\frac{1-\frac{J_0}{G_0}\omega^2+\frac{D_0}{G_0}k_1^2}{(k_1^2+k_2^2)\,ik_1}e^{-ik_1|x|} - \frac{1}{2D_0}\frac{1-\frac{J_0}{G_0}\omega^2-\frac{D_0}{G_0}k_2^2}{(k_1^2+k_2^2)\,k_2}e^{-k_2|x|}. \tag{A.4}$$

More generally, the displacement response $w(\omega, x)$ for different types of sources is given as:

$$\begin{aligned} w(\omega,x) &= \frac{1}{2D_0(k_1^2+k_2^2)}\left(e^{-ik_1|x|}-e^{-k_2|x|}\right)\mathrm{sgn}(x), && \text{for } q\neq 0,\\ w(\omega,x) &= \frac{ik_1}{2(k_1^2+k_2^2)}e^{-ik_1|x|} - \frac{k_2}{2(k_1^2+k_2^2)}e^{-k_2|x|}, && \text{for } p\neq 0,\\ w(\omega,x) &= \frac{-D_0k_1^2+J_0\omega^2}{2D_0(k_1^2+k_2^2)}e^{-ik_1|x|}\,\mathrm{sgn}(x) - \frac{D_0k_2^2+J_0\omega^2}{2D_0(k_1^2+k_2^2)}e^{-k_2|x|}\,\mathrm{sgn}(x), && \text{for } s\neq 0. \end{aligned} \tag{A.5}$$

A.2. The Green's function

Because the system preserves the translational symmetry, applying the linear combination of the four type point load $f_0\delta(x-x')$, $q_0\delta(x-x')$, $p_0\delta(x-x')$, and $s_0\delta(x-x')$ at x' simultaneously, the displacement response function responded at x is

$$w(x',x) = \mathbf{B}_1(x-x')^T\mathbf{Q}_0 e^{-ik_1|x-x'|} + \mathbf{B}_2(x-x')^T\mathbf{Q}_0 e^{-k_2|x-x'|} \tag{A.6}$$

where

$$\mathbf{B}_1(x) = \begin{bmatrix} A_1 \\ \mathrm{sgn}(x-x')A_2 \\ A_3 \\ \mathrm{sgn}(x-x')A_4 \end{bmatrix}, \quad \mathbf{B}_2(x) = \begin{bmatrix} A_1a_1 \\ \mathrm{sign}(x-x')A_2a_2 \\ A_3a_3 \\ \mathrm{sign}(x)A_4a_4 \end{bmatrix} \quad \mathbf{Q}_0 = \begin{bmatrix} p_0 \\ s_0 \\ f_0 \\ q_0 \end{bmatrix}, \tag{A.7}$$

and

$$\begin{aligned} A_1 &= \frac{ik_1}{2(k_1^2+k_2^2)}, & a_1 &= -\frac{k_2}{ik_1}, \\ A_2 &= \frac{D_0k_1^2 - J_0\omega^2}{2D_0(k_1^2+k_2^2)}, & a_2 &= \frac{D_0k_2^2 + J_0\omega^2}{D_0k_1^2 - J_0\omega^2}, \\ A_3 &= \frac{1}{2D_0}\frac{1-\frac{J_0}{G_0}\omega^2+\frac{D_0}{G_0}k_1^2}{(k_1^2+k_2^2)ik_1}, & a_3 &= -\frac{ik_1}{k_2}\frac{1-\frac{J_0}{G_0}\omega^2-\frac{D_0}{G_0}k_2^2}{1-\frac{J_0}{G_0}\omega^2+\frac{D_0}{G_0}k_1^2}, \\ A_4 &= \frac{1}{2D_0(k_1^2+k_2^2)}, & a_4 &= -1. \end{aligned} \tag{A.8}$$

Meanwhile, the response functions $\psi(x',x)$, $F(x',x)$, and $M(x',x)$ can be assumed as

$$\begin{aligned} \psi(x',x) &= R_\psi^1(x-x')\mathbf{B}_1(x-x')^T\mathbf{Q}(x')e^{-ik_1|x-x'|} + R_\psi^2(x-x')\mathbf{B_2}(x-x')^T\mathbf{Q}(x')e^{-k_2|x-x'|} \\ F(x',x) &= R_F^1(x-x')\mathbf{B_1}(x-x')^\mathbf{T}\mathbf{Q}(x')e^{-ik_1|x-x'|} + R_F^2(x-x')\mathbf{B_2}(x-x')^\mathbf{T}\mathbf{Q}(x')e^{-k_2|x-x'|} \\ M(x',x) &= R_M^1(x-x')\mathbf{B_1}(x-x')^T\mathbf{Q}(x')e^{-ik_1|x-x'|} + R_M^2(x-x')\mathbf{B_2}(x-x')^T\mathbf{Q}(x')e^{-k_2|x-x'|} \end{aligned} \tag{A.9}$$

Inserting them into the first three equations of Eq. (A.1) with the aid of Eq. (A.6), we obtain the following linear equations

$$\begin{aligned} &-\mathrm{sgn}(x-x')ik_1R_\psi^1(x-x') + \frac{R_M^1(x-x')}{D_0} = 0 \\ &R_\psi^1(x-x') + \frac{R_F^1(x-x')}{G_0} = -\mathrm{sgn}(x-x')ik_1 \\ &-\mathrm{sgn}(x-x')ik_1R_F^1(x-x') = -\rho_0\omega^2 \end{aligned} \tag{A.10}$$

for $R_\psi^1(x-x')$, $R_F^1(x-x')$, $R_M^1(x-x')$, and the linear equations

$$\begin{aligned} &-\mathrm{sgn}(x-x')k_2R_\psi^2(x-x') + \frac{R_M^2(x-x')}{D_0} = 0 \\ &R_\psi^2(x-x') + \frac{R_F^2(x-x')}{G_0} = -\mathrm{sgn}(x-x')k_2 \\ &-\mathrm{sgn}(x-x')k_2R_F^2(x-x') = -\rho_0\omega^2 \end{aligned} \tag{A.11}$$

for $R_\psi^2(x-x')$, $R_F^2(x-x')$, $R_M^2(x-x')$. Solving these equations yields $R_\psi^1(x-x')$, $R_F^1(x-x')$, $R_M^1(x-x')$, as well as $R_\psi^2(x-x')$, $R_F^2(x-x')$, and $R_M^2(x-x')$.

Therefore, the Green's function in the frequency domain is

$$\mathbf{G}(\omega, x-x') = \mathbf{R}_1(x-x')\mathbf{B}_1(x-x')^T e^{-ik_1|x-x'|} + \mathbf{R}_2(x-x')\mathbf{B}_2(x-x')^T e^{-k_2|x-x'|} \tag{A.12}$$

and

$$\mathbf{R}_1(x) = \begin{bmatrix} R_M^1(x) \\ R_F^1(x) \\ 1 \\ R_\psi^1(x) \end{bmatrix}, \quad \mathbf{R}_2(x) = \begin{bmatrix} R_M^2(x) \\ R_F^2(x) \\ 1 \\ R_\psi^2(x) \end{bmatrix}. \tag{A.13}$$

And the state vector response $\mathbf{u}(x)$ at x, excited by a actuation vector $\mathbf{Q}(x')$ at x', is given by

$$\mathbf{u}(x) = \int \mathbf{G}(\omega, x-x')\mathbf{Q}(x')dx'. \tag{A.14}$$

A.3. Symmetry conditions of the Green's function

In this section, we analyze the symmetry properties of the Green's function. The Green's function $\mathbf{G}(\omega, k)$ satisfies the following relation from Eq. (4):

$$\boldsymbol{\zeta}(\omega, k)\,\mathbf{G}(\omega, k) = \mathbf{I}, \tag{A.15}$$

where the analytical expression of $\mathbf{G}(\omega, k)$ is provided in Eq. (A.12). Owing to the symmetry condition of $\boldsymbol{\zeta}(\omega, k)$ given in Eq. (6), the Green's function also satisfies the following symmetries for a given ω and k:

$$\mathbf{G}(\omega, k) = \mathbf{G}^{*}(-\omega, -k), \quad \mathbf{G}(\omega, k) = \mathbf{G}^{T}(-\omega, -k), \quad \mathbf{G}(\omega, k) = \mathbf{G}(-\omega, k). \tag{A.16}$$

The Green's function in real space is given by the inverse Fourier transform:

$$\mathbf{G}(\omega, x - x') = \frac{1}{\sqrt{2\pi}} \int_{-\infty}^{\infty} \mathbf{G}(\omega, k)\, e^{ik(x-x')}\, dk, \tag{A.17}$$

and satisfies the following symmetry relations:

$$\mathbf{G}(\omega, x - x') = \mathbf{G}^{*}(-\omega, x' - x), \quad \mathbf{G}(\omega, x - x') = \mathbf{G}^{T}(-\omega, x' - x), \quad \mathbf{G}(\omega, x - x') = \mathbf{G}(-\omega, x' - x). \tag{A.18}$$

A.4. The asymptotic Green's function of Willis effective model

The Green's function in frequency-wavenumber domain is

$$\mathbf{H}(\omega, k)\mathbf{G}_{\mathrm{eff}}(\omega, k) = \mathbf{I} \tag{A.19}$$

Therefore, the Green's function in the frequency-space domain is

$$\mathbf{G}_{\mathrm{eff}}(\omega, x - x') = \frac{1}{\sqrt{2\pi}} \int_{-\infty}^{\infty} \frac{e^{ik(x-x')}}{\mathbf{H}(\omega, k)} dk = \frac{1}{\sqrt{2\pi}} \int_{-\infty}^{\infty} \mathbf{G}_{\mathrm{eff}}(\omega, k) e^{ik(x-x')} dk \tag{A.20}$$

Using the residue theorem, we have

$$\mathbf{G}_{\mathrm{eff}}(\omega, x - x') = \begin{cases} \frac{1}{\sqrt{2\pi}} \sum_{n=1}^{2} \mathbf{G}_{\mathrm{eff}}(\omega, k_n) e^{ik_n(x-x')}, & x - x' > 0 \\ \frac{1}{\sqrt{2\pi}} \sum_{n=3}^{4} \mathbf{G}_{\mathrm{eff}}(\omega, k_n) e^{ik_n(x-x')}, & x - x' < 0 \end{cases} \tag{A.21}$$

If beam length L is large, the term with a larger imaginary part can be neglected for $x - x' > 0$ while the term with a smaller imaginary part can be neglected for $x - x' < 0$. Then we have the following asymptotic relation

$$\mathbf{G}_{\mathrm{eff}}(\omega, x - x') \sim \begin{cases} \frac{1}{\sqrt{2\pi}} \mathbf{G}_{\mathrm{eff}}(\omega, k_1) e^{ik_1(x-x')}, & x - x' > 0 \\ \frac{1}{\sqrt{2\pi}} \mathbf{G}_{\mathrm{eff}}(\omega, k_3) e^{ik_3(x-x')}, & x - x' < 0 \end{cases} \tag{A.22}$$

For a unit shear force $\mathbf{Q}^{1}_{\mathrm{ext}}(x) = [0, 0, 0, 1]^{T}\delta(x)$ is applied at $x = 0$ and a unit shear force $\mathbf{Q}^{2}_{\mathrm{ext}}(x) = [0, 0, 0, 1]^{T}\delta(x - L)$ is applied at $x = L$, we have

$$\Delta = G^{11}_{\mathrm{eff}}(\omega, L) - G^{11}_{\mathrm{eff}}(\omega, -L) \sim \frac{1}{\sqrt{2\pi}} G^{11}_{\mathrm{eff}}\left(\omega, k_1\right) e^{ik_1 L}. \tag{A.23}$$

Appendix B. Derivation of effective constitutive relations

Substituting Eq. (7) into Eq. (15) gives

$$\boldsymbol{\zeta}\left(\mathbf{u}_{\mathrm{eff}} - \mathbf{u}_{\mathrm{h}}\right) = -\mathbf{Q}_{\mathrm{eff}}. \tag{B.1}$$

Additionally, injecting Eq. (11) into Eq. (8) to eliminate the local state vector $\mathbf{u}_{\mathrm{loc}}$ yields

$$\left(\mathbf{I} - \boldsymbol{\beta}\tilde{\mathbf{S}}\right)\mathbf{Q}_0 = \boldsymbol{\beta}\mathbf{u}_{\mathrm{h}}, \tag{B.2}$$

where $\mathbf{I}$ is the 4×4 identity matrix. The $\boldsymbol{\zeta}$ is not a singular matrix in general, so Eq. (B.1) can be rewritten as

$$\mathbf{u}_{\mathrm{h}} = \mathbf{u}_{\mathrm{eff}} + \boldsymbol{\zeta}^{-1}\mathbf{Q}_{\mathrm{eff}}. \tag{B.3}$$

In addition, through the elimination of the local actuation vector $\mathbf{Q}_0$ in Eq. (B.2) and Eq. (16), we find

$$\boldsymbol{\beta}\mathbf{u}_{\mathrm{h}} = \left(\mathbf{I} - \boldsymbol{\beta}\tilde{\mathbf{S}}\right)\mathbf{Q}_{\mathrm{eff}} l. \tag{B.4}$$

Subtracting Eq. (B.4) by the product of $\boldsymbol{\beta}$ to Eq. (B.3) gives

$$\boldsymbol{\beta}\left(\mathbf{u}_{\mathrm{eff}} + \boldsymbol{\zeta}^{-1}\mathbf{Q}_{\mathrm{eff}}\right) = \left(\mathbf{I} - \boldsymbol{\beta}\tilde{\mathbf{S}}\right)\mathbf{Q}_{\mathrm{eff}} l. \tag{B.5}$$

Reorganizing yields the effective constitutive relations in Eq. (17)

$$\mathbf{Q}_{\mathrm{eff}} = \left[\left(\mathbf{I} - \boldsymbol{\beta}\tilde{\mathbf{S}}\right) l - \boldsymbol{\beta}\boldsymbol{\zeta}^{-1}\right]^{-1} \boldsymbol{\beta}\mathbf{u}_{\mathrm{eff}}. \tag{B.6}$$

Appendix C. Interpretation of nonlocal effective parameters

According to our effective medium theory, the effective parameters in Eq. (17) depend on both frequency and wavenumber. However, for freely propagating waves, frequency and wavenumber are not independent but must satisfy the dispersion relation given in Eq. (36). This implies that the effective parameters are physically meaningful only at frequencies and wavenumbers that lie on the dispersion curves corresponding to freely traveling waves. This raises an apparent paradox: whether the effective parameters remain meaningful for arbitrary frequency and wavenumber, or whether the assumption of independent frequency and wavenumber in the effective parameters requires further justification.

To treat frequency and wavenumber as independent variables, we must consider waves under external excitation. We begin by introducing a traveling wave excitation of the form

$$\mathbf{Q}_{\text{ext}}(x,t) = \mathbf{Q}_{\text{ext}}(\omega,k)e^{i(kx-\omega t)} \tag{C.1}$$

where $\mathbf{Q}_{\text{ext}}(\omega,k)$ represents the amplitude, which depends on both frequency and wavenumber. The solution to Eq. (33) can then be expressed as

$$\mathbf{u}_{\text{eff}}(x,t) = \mathbf{u}_{\text{eff}}(\omega,k)e^{i(kx-\omega t)} \tag{C.2}$$

where the amplitude vector satisfies

$$\mathbf{u}_{\text{eff}}(\omega,k) = \mathbf{H}(\omega,k)^{-1}\mathbf{Q}_{\text{ext}}(\omega,k). \tag{C.3}$$

If the frequency and wavenumber satisfy the dispersion relation, $\mathbf{H}(\omega,k)$ becomes singular, causing the amplitude vector to diverge, similar to resonance in vibrational systems. To eliminate this singularity, damping can be introduced into the system, ensuring that the amplitude vector remains finite. Conversely, if the frequency and wavenumber do not satisfy the dispersion relation, $\mathbf{H}(\omega,k)$ remains nonsingular, and the amplitude vector is naturally finite. In this case, the amplitude vector depends on $\mathbf{H}(\omega,k)$, which in turn is determined by the effective parameters, allowing frequency and wavenumber to be treated as independent variables.

Next, we consider a more realistic harmonic excitation of the form

$$\mathbf{Q}_{\text{ext}}(x,t) = \mathbf{Q}_{\text{ext}}(\omega,x)e^{-i\omega t}, \tag{C.4}$$

which can be expanded as

$$\mathbf{Q}_{\text{ext}}(\omega,x) = \frac{e^{-i\omega t}}{\sqrt{2\pi}}\int_{-\infty}^{\infty}\mathbf{Q}_{\text{ext}}(\omega,k)e^{ikx}dk. \tag{C.5}$$

For each Fourier component $\mathbf{Q}_{\text{ext}}(\omega,k)$, the corresponding response is given by $\mathbf{u}_{\text{eff}}(\omega,k)$. Using the principle of superposition, the total response can be written as

$$\mathbf{u}_{\text{eff}}(t,x) = \frac{e^{-i\omega t}}{\sqrt{2\pi}}\int_{-\infty}^{\infty}\mathbf{H}(\omega,k)^{-1}\mathbf{Q}_{\text{ext}}(\omega,k)e^{ikx}dk. \tag{C.6}$$

This result shows that the state vector response depends on the effective parameters for arbitrary frequency and wavenumber. Therefore, in the context of excitation problems, frequency and wavenumber can be treated as independent variables. Furthermore, this approach offers greater flexibility in modulating the effective parameters, as both frequency and wavenumber can be controlled. For example, a gradient medium with slowly varying properties can be designed using the WKB approximation to develop an elastic ray theory, enabling novel wave propagation phenomena (Wang et al., 2023).

Appendix D. Geometric and material parameters

The geometric parameters of the model are shown in Fig. D.11 and their values are listed in Table D.1. The host beam is made of aluminum with a Young's modulus of 70 GPa, a Poisson ratio of 0.33, and a density of 2700 kg/m^3. The piezoelectric patches are composed of PZT-5H, with material properties available in the COMSOL material library. The capacitor C_0 in Eq. (38) has a value of 0.611 pF.

Table D.1
Geometry parameters and their values of the unit cell.

Parameter	Value (Unit)	Parameter	Value (Unit)
w	21.9 mm	l	20 mm
w_1	16.1 mm	l_1	12 mm
w_2	8 mm	l_2	4 mm
w_3	3.5 mm	l_3	2.9 mm
h_b	2 mm	h_p	0.5 mm

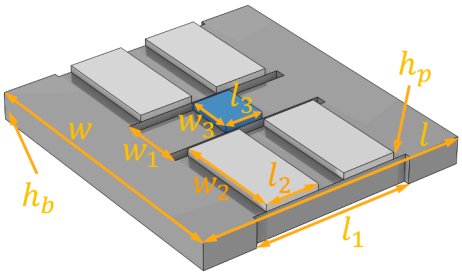

Fig. D.11. Geometric parameters of the unit cell.

Appendix E. Description of transfer function g and feedforward control loop

In practical implementation, a feedforward control strategy is employed to realize the transfer functions in Eq. (38). The schematic of the feedforward control loop is shown in Fig. E.12. As illustrated, the piezoelectric sensor captures the voltage induced by the incident wave. This signal is corrected by subtracting the feedback contributions from the actuators at two summing nodes. The resulting signal is passed through a low-pass filter and then fed into a digital control unit, which includes a band-pass filter and three internal transfer functions h_1, h_2, and g, connected via two subtraction loops. The outputs from the digital controller are applied to the two actuator groups.

We now demonstrate that this feedforward architecture is mathematically equivalent to the transfer relation in Eq. (38):

$$\begin{aligned} V_{a1} &= h_1\left(V_s - gV_{a1} - gV_{a2}\right), \\ V_{a2} &= h_2\left(V_s - gV_{a1} - gV_{a2}\right). \end{aligned} \tag{E.1}$$

Solving these equations yields:

$$\begin{aligned} V_{a1} &= H_1 V_s, \\ V_{a2} &= H_2 V_s, \end{aligned} \tag{E.2}$$

where the realized transfer functions H_1 and H_2 are related to the internal controller parameters by:

$$H_1 = \frac{h_1}{1 + g(h_1 + h_2)}, \quad H_2 = \frac{h_2}{1 + g(h_1 + h_2)}. \tag{E.3}$$

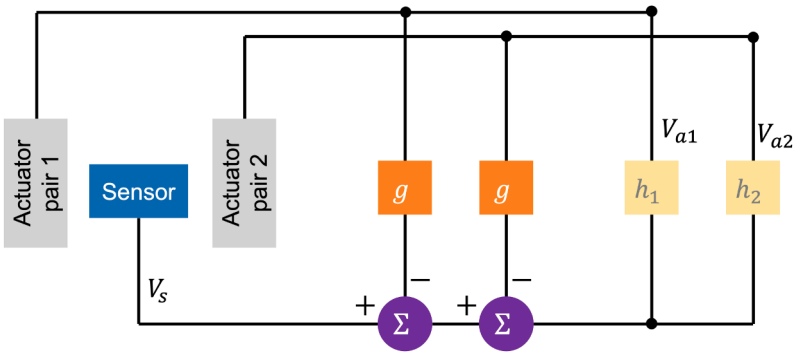

Fig. E.12. Diagram of the feedforward control loop.

To implement the feedback transfer function g, a rational-form function is first specified. Its parameters are identified experimentally by applying voltages to the actuators and measuring the resulting voltage at the sensor, allowing g to accurately emulate the mechanical feedback path. In our study, we first specify H_1 and H_2 as design targets, which can be directly implemented in COMSOL simulations as nonlocal algebraic coupling relations. In COMSOL, this is implemented using the Global ODEs and DAEs interface. The sensor electrodes have their bottom and top surfaces grounded, and a nonlocal operator is defined on the top surface to extract the sensor voltage V_s

$$V_s = \frac{1}{C_0}\int_A D_z \, dA \tag{E.4}$$

where $C_0 = 1$ nF and A is the area on the top surface, and D_z is the z-component of electric displacement vector. The global algebraic relations

$$V_1 = H_1 V_s, \quad V_2 = H_2 V_s \tag{E.5}$$

are then imposed directly in the Global ODEs/DAEs module. The bottom surfaces of all actuators are grounded; the voltages V_1 and V_2 obtained from the algebraic equations are applied to the top surfaces of the left and right actuator pairs, respectively. This procedure enforces the required nonlocal algebraic coupling between sensing and actuation.

To realize these target transfer functions experimentally, the corresponding internal parameters h_1 and h_2 must be computed using Eq. (E.3) inversely, enabling the desired control behavior to be physically implemented through the feedforward control loop.

Appendix F. Retrieval of local polarizability tensor

Due to the complexity of the unit cell geometry, accurately relating the local polarizability tensor $\boldsymbol{\beta}$ to the transfer functions $H_1(\omega)$ and $H_2(\omega)$ analytically is challenging. In this section, we employ a retrieval method to numerically extract the local polarizability tensor, as illustrated in Fig. F.13(a). The local state vector $\mathbf{u}_{\text{loc}}$ is directly obtained from COMSOL, while the local actuation vector $\mathbf{Q}$ is extracted using the scattering method. For each test, given the known $\mathbf{u}_{\text{loc}}$ and $\mathbf{Q}$, we obtain four equations from Eq. (8) with $\boldsymbol{\beta}$ as the unknown. Since the polarizability tensor contains 16 unknowns, four independent scattering tests are conducted to construct a system of 16 equations, enabling the unique determination of these unknowns.

F.1. Numerical extraction of the local actuation vector

Here, we utilize the extracted displacement field in the frequency domain to inversely determine the local actuation vector $\mathbf{Q}$. A unit cell is embedded in the middle of the host beam, with perfect matching layers on both sides (not shown). A unit transverse force is applied at a specified position in the host beam, as illustrated in Fig. F.13(a). In this section, we use asymmetric constant transfer function with $H_1(\omega) = 0.35$ and $H_2(\omega) = -0.25$. According to Eq. (A.6), the analytical displacement response function at position x for an excitation applied at the origin is given by

$$w(0,x) = \mathbf{B}_1(x)^T \mathbf{Q}_0 e^{-ik_1|x|} + \mathbf{B}_2(x)^T \mathbf{Q}_0 e^{-k_2|\mathbf{x}|}. \tag{F.1}$$

Meanwhile, the scattered displacement field is extracted from COMSOL. For each test, we perform two simulations: one with the transfer function set to zero and another with a nonzero transfer function. The scattered displacement field is then obtained by subtracting the displacement field of the zero-transfer-function case from that of the nonzero-transfer-function case. For the ith test, we acquire the scattered displacement vector $\mathbf{w}^i = [w^i(0,x_1), \dots, w^i(0,x_N)]^T$ at positions $\mathbf{x} = [x_1, x_2, \dots, x_N]^T$. At each position, Eq. (F.1) must be satisfied, leading to

$$\begin{aligned}
&\left[\mathbf{B}_1(x_1)^T e^{-ik_1|x_1|} + \mathbf{B}_2(x_1)^T e^{-k_2|x_1|}\right]\mathbf{Q}^i = w^i(0,x_1)\\
&\left[\mathbf{B}_1(x_2)^T e^{-ik_1|x_2|} + \mathbf{B}_2(x_2)^T e^{-k_2|x_2|}\right]\mathbf{Q}^i = w^i(0,x_2)\\
&\qquad\qquad\qquad\cdots\\
&\left[\mathbf{B}_1(x_N)^T e^{-ik_1|x_N|} + \mathbf{B}_2(x_N)^T e^{-k_2|x_N|}\right]\mathbf{Q}^i = w^i(0,x_N).
\end{aligned} \tag{F.2}$$

Here, N is chosen to be greater than 4, and $\mathbf{Q}^i$ is determined using the least squares method. To achieve the desired precision, a large integer N (2000 in this study) is selected. By solving the overdetermined system using the least squares method, we obtain

$$\mathbf{Q}^i = \mathcal{G}^{-1}\mathbf{w}^i \tag{F.3}$$

where $(\cdot)^{-1}$ denotes the Moore-Penrose pseudoinverse, and the rectangular matrix $\mathcal{G}$ is defined as

$$\mathcal{G} = \begin{bmatrix}
\mathbf{B}_1(x_1)^T e^{-ik_1|x_1|} + \mathbf{B}_2(x_1)^T e^{-k_2|x_1|}\\
\mathbf{B}_1(x_2)^T e^{-ik_1|x_2|} + \mathbf{B}_2(x_2)^T e^{-k_2|x_2|}\\
\cdots\\
\mathbf{B}_1(x_N)^T e^{-ik_1|x_N|} + \mathbf{B}_2(x_N)^T e^{-k_2|x_N|}
\end{bmatrix} \tag{F.4}$$

To assess the accuracy of the inverse extraction, we compare the analytical scattered displacement field, computed using Eq. (F.1) with the inversely obtained $\mathbf{Q}^i$, against the scattered displacement field extracted from the COMSOL simulation for the first case, as shown in Fig. F.13(b). The real and imaginary parts of both results closely match, except in the region very close to the unit cell, where microstructural effects become significant. This confirms that the point source assumption is valid for our study and that the inverse extraction method is reliable.

F.2. Numerical extraction of the polarizability tensor

Now we have four local actuation vectors for four tests. The four local state vectors can be extracted in COMOSL directly. Therefore, for these four tests, the following condition is satisfied according to Eq. (8)

$$\mathbf{Q}^i = \boldsymbol{\beta}\mathbf{u}^i_{\text{loc}}, \quad i = 1,2,3,4, \tag{F.5}$$

These linear equations can also be expressed as:

$$\mathbf{Q}^i = u^i_{\text{loc}}(1)\boldsymbol{\beta}_1 + u^i_{\text{loc}}(2)\boldsymbol{\beta}_2 + u^i_{\text{loc}}(3)\boldsymbol{\beta}_3 + u^i_{\text{loc}}(4)\boldsymbol{\beta}_4, \quad i = 1,2,3,4, \tag{F.6}$$

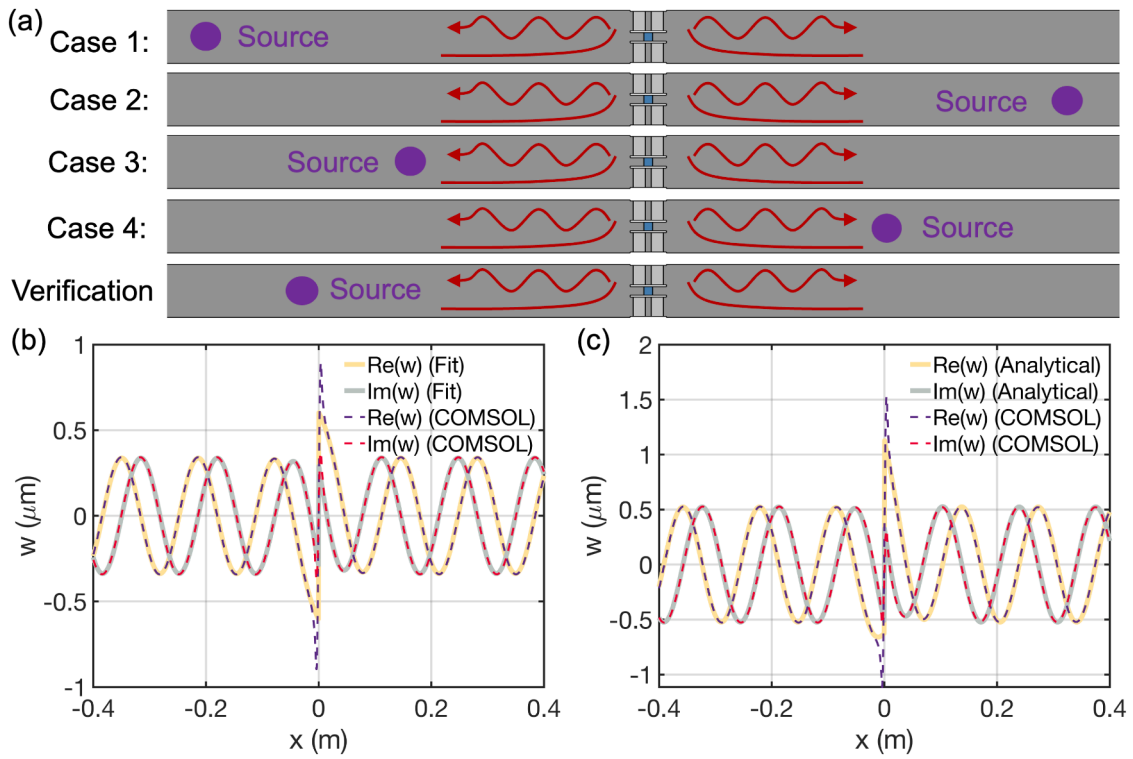

Fig. F.13. Numerical extraction of the polarizability tensor. (a) Four numerical tests for extracting the polarizability tensor, along with an additional case for verification. (b) Real part (purple dashed line) and imaginary part (red dashed line) of the scattered displacement field from COMSOL simulations for the first case in (a), compared with the fitted response of a point source (yellow solid line for the real part and gray solid line for the imaginary part). (c) Real part (purple dashed line) and imaginary part (red dashed line) of the scattered displacement field from COMSOL simulations for the verification case in (a), compared with the analytical response of a point source derived from the four tests in (a) (yellow solid line for the real part and gray solid line for the imaginary part).

where $\boldsymbol{\beta}_j$ $(j = 1, 2, 3, 4)$ is the jth column vector of the matrix $\boldsymbol{\beta}$, and $u^i_{\text{loc}}(j)$ $(j = 1, 2, 3, 4)$ is the jth element of the vector $\mathbf{u}^i_{\text{loc}}$. Eq. (F.6) can be reformulated as:

$$\begin{bmatrix} \mathbf{Q}^1 \\ \mathbf{Q}^2 \\ \mathbf{Q}^3 \\ \mathbf{Q}^4 \end{bmatrix} = \begin{bmatrix} u^1_{\text{loc}}(1)\mathbf{I} & u^1_{\text{loc}}(2)\mathbf{I} & u^1_{\text{loc}}(3)\mathbf{I} & u^1_{\text{loc}}(4)\mathbf{I} \\ u^2_{\text{loc}}(1)\mathbf{I} & u^2_{\text{loc}}(2)\mathbf{I} & u^2_{\text{loc}}(3)\mathbf{I} & u^2_{\text{loc}}(4)\mathbf{I} \\ u^3_{\text{loc}}(1)\mathbf{I} & u^3_{\text{loc}}(2)\mathbf{I} & u^3_{\text{loc}}(3)\mathbf{I} & u^3_{\text{loc}}(4)\mathbf{I} \\ u^4_{\text{loc}}(1)\mathbf{I} & u^4_{\text{loc}}(2)\mathbf{I} & u^4_{\text{loc}}(3)\mathbf{I} & u^4_{\text{loc}}(4)\mathbf{I} \end{bmatrix} \begin{bmatrix} \boldsymbol{\beta}_1 \\ \boldsymbol{\beta}_2 \\ \boldsymbol{\beta}_3 \\ \boldsymbol{\beta}_4 \end{bmatrix}, \tag{F.7}$$

where $\mathbf{I}$ is the 4×4 identity matrix. We concatenate $\mathbf{Q}^i$ and $\boldsymbol{\beta}_i$ $(i = 1, 2, 3, 4)$ to form larger vectors and assemble $\mathbf{u}^i_{\text{loc}}$ $(i = 1, 2, 3, 4)$ into a matrix

$$\mathcal{Q} = \begin{bmatrix} \mathbf{Q}^1 \\ \mathbf{Q}^2 \\ \mathbf{Q}^3 \\ \mathbf{Q}^4 \end{bmatrix}, \quad \mathcal{U}_{\text{loc}} = \begin{bmatrix} \left(\mathbf{u}^1_{\text{loc}}\right)^T \\ \left(\mathbf{u}^2_{\text{loc}}\right)^T \\ \left(\mathbf{u}^3_{\text{loc}}\right)^T \\ \left(\mathbf{u}^4_{\text{loc}}\right)^T \end{bmatrix}, \quad \mathcal{B} = \begin{bmatrix} \boldsymbol{\beta}_1 \\ \boldsymbol{\beta}_2 \\ \boldsymbol{\beta}_3 \\ \boldsymbol{\beta}_4 \end{bmatrix}. \tag{F.8}$$

Then Eq. (F.7) can be expressed as

$$\mathcal{Q} = \mathcal{U}_{\text{loc}} \otimes \mathbf{I}\mathcal{B}, \tag{F.9}$$

where $\otimes$ is the Kronecker product. Solving for $\mathcal{B}$, we obtain

$$\mathcal{B} = \left(\mathcal{U}_{\text{loc}} \otimes \mathbf{I}\right)^{-1} \mathcal{Q} \tag{F.10}$$

Finally, the local polarizability matrix $\boldsymbol{\beta}$ is obtained by rearranging the elements of the vector $\mathcal{B}$. Since the polarizability matrix is generally frequency-dependent, we conduct these four tests at different frequencies and derive the frequency-dependent polarizability matrix function through curve fitting.

Finally, we verify the local polarizability matrix $\boldsymbol{\beta}$ through a validation test, as shown in Fig. F.13(c). In this case, the source position differs from those in the four previous cases. First, the local state vector is extracted, and then the local actuation vector is determined by multiplying the local state vector by the local polarizability matrix. Using Eq. (F.1), the analytical scattered displacement field is then computed for the obtained local actuation vector. This analytical result is compared with the scattered displacement field extracted from the COMSOL simulation in Fig. F.13(c). The consistency between the two results confirms the validity of the point source assumption and the reliability of the retrieval method for determining the polarizability matrix.

Appendix G. Parity symmetry analysis

Symmetry analysis of macroscopic media

In classical physics, a parity transformation refers to a spatial inversion that changes the sign of spatial coordinates. In one dimension, it is equivalent to the reflection or mirror transformation. Mathematically, it is expressed as

$$x \xrightarrow{\mathcal{P}} -x. \tag{G.1}$$

where $\mathcal{P}$ denotes the parity transformation. In the reciprocal space, it can be expressed as

$$k \xrightarrow{\mathcal{P}} -k. \tag{G.2}$$

Since $M_{\text{eff}}(\omega,k)$, $\mu_{\text{eff}}(\omega,k)$, $\kappa_{\text{eff}}(\omega,k)$, and $\gamma_{\text{eff}}(\omega,k)$ are symmetric with respect to $x=0$, while $F_{\text{eff}}(\omega,k)$, $J_{\text{eff}}(\omega,k)$, $\gamma_{\text{eff}}(\omega,k)$, and $\varphi_{\text{eff}}(\omega,k)$ are antisymmetric with respect to $x=0$, it follows that $M_{\text{eff}}(\omega,k)$, $\mu_{\text{eff}}(\omega,k)$, $\kappa_{\text{eff}}(\omega,k)$, and $\gamma_{\text{eff}}(\omega,k)$ have even parity, whereas $F_{\text{eff}}(\omega,k)$, $J_{\text{eff}}(\omega,k)$, $\gamma_{\text{eff}}(\omega,k)$, and $\varphi_{\text{eff}}(\omega,k)$ have odd parity. This can be expressed as

$$\begin{aligned}
&M_{\text{eff}}(\omega,k)\xrightarrow{\mathcal{P}} M_{\text{eff}}(\omega,-k), \quad && \kappa_{\text{eff}}(\omega,k)\xrightarrow{\mathcal{P}} \kappa_{\text{eff}}(\omega,-k),\\
&F_{\text{eff}}(\omega,k)\xrightarrow{\mathcal{P}} -F_{\text{eff}}(\omega,-k), && \gamma_{\text{eff}}(\omega,k)\xrightarrow{\mathcal{P}} -\gamma_{\text{eff}}(\omega,-k),\\
&\mu_{\text{eff}}(\omega,k)\xrightarrow{\mathcal{P}} \mu_{\text{eff}}(\omega,-k), && \upsilon_{\text{eff}}(\omega,k)\xrightarrow{\mathcal{P}} \upsilon_{\text{eff}}(\omega,-k),\\
&J_{\text{eff}}(\omega,k)\xrightarrow{\mathcal{P}} -J_{\text{eff}}(\omega,-k), && \varphi_{\text{eff}}(\omega,k)\xrightarrow{\mathcal{P}} -\varphi_{\text{eff}}(\omega,-k).
\end{aligned} \tag{G.3}$$

We define $\boldsymbol{\mathcal{E}} = [\boldsymbol{\varepsilon}, \mathbf{p}]^T$, $\boldsymbol{\Sigma} = [\boldsymbol{\sigma}, \mathbf{v}]^T$ and constitutive relation in Eq. (24) as

$$\boldsymbol{\mathcal{E}} = \boldsymbol{\mathcal{S}}\boldsymbol{\Sigma}. \tag{G.4}$$

It can be rewritten as the matrix form

$$\boldsymbol{\Sigma}(\omega,-k) = \mathbf{P}\boldsymbol{\Sigma}(\omega,k), \quad \boldsymbol{\mathcal{E}}(\omega,-k) = \mathbf{P}\boldsymbol{\mathcal{E}}(\omega,k) \tag{G.5}$$

where κ is the complex conjugation operator and

$$\mathbf{P} = \begin{bmatrix} 1 & 0 & 0 & 0 \\ 0 & -1 & 0 & 0 \\ 0 & 0 & 1 & 0 \\ 0 & 0 & 0 & -1 \end{bmatrix} \tag{G.6}$$

For the system with parity symmetry, the governing equations of a system must remain form-invariant under parity symmetry. Therefore, we have the following equations after parity transformation

$$\boldsymbol{\mathcal{E}}(\omega,-k) = \boldsymbol{\mathcal{S}}(\omega,-k)\boldsymbol{\Sigma}(\omega,-k) \tag{G.7}$$

Therefore, we have

$$\boldsymbol{\mathcal{S}}(\omega,-k) = \mathbf{P}\boldsymbol{\mathcal{S}}(\omega,k)\mathbf{P}^{-1} \tag{G.8}$$

Substituting Eq. (G.6) into Eq. (G.8), we have

$$\boldsymbol{\mathcal{S}}(\omega,-k) = \begin{bmatrix} S_{11}(\omega,k) & -S_{12}(\omega,k) & S_{13}(\omega,k) & -S_{14}(\omega,k) \\ -S_{21}(\omega,k) & S_{22}(\omega,k) & -S_{23}(\omega,k) & S_{24}(\omega,k) \\ S_{31}(\omega,k) & -S_{32}(\omega,k) & S_{33}(\omega,k) & -S_{34}(\omega,k) \\ -S_{41}(\omega,k) & S_{42}(\omega,k) & -S_{43}(\omega,k) & S_{44}(\omega,k) \end{bmatrix} \tag{G.9}$$

If parity symmetry is preserved, $\boldsymbol{\mathcal{S}}(\omega,-k)$ must be equal to $\boldsymbol{\mathcal{S}}(\omega,k)$, leading to the result

$$\begin{aligned}
&S_{11}(\omega,-k) = S_{11}(\omega,k), && S_{12}(\omega,-k) = -S_{12}(\omega,k), && S_{13}(\omega,-k) = S_{13}(\omega,k) && S_{14}(\omega,-k) = -S_{14}(\omega,k),\\
&S_{21}(\omega,-k) = -S_{21}(\omega,k), && S_{22}(\omega,-k) = S_{22}(\omega,k), && S_{23}(\omega,-k) = -S_{23}(\omega,k), && S_{24}(\omega,-k) = S_{24}(\omega,k),\\
&S_{31}(\omega,-k) = S_{31}(\omega,k), && S_{32}(\omega,-k) = -S_{32}(\omega,k), && S_{33}(\omega,-k) = S_{33}(\omega,k), && S_{34}(\omega,-k) = -S_{34}(\omega,k),\\
&S_{41}(\omega,-k) = -S_{41}(\omega,k), && S_{42}(\omega,-k) = S_{42}(\omega,k), && S_{43}(\omega,-k) = -S_{43}(\omega,k), && S_{44}(\omega,-k) = S_{44}(\omega,k).
\end{aligned} \tag{G.10}$$

With parity symmetry, the nonlocal Willis couplings ($k \neq 0$) can still be nonzero but must satisfy the symmetry conditions given in Eq. (G.10). This contrasts with the case of a local Willis metabeam ($k = 0$), where broken parity is necessary for the emergence of Willis couplings (Liu et al., 2019). Under long wave condition $k \to 0$, antisymmetric coefficients must vanish and we obtain

$$\mathcal{S}_{12}(\omega) = \mathcal{S}_{13}(\omega) = \mathcal{S}_{21}(\omega) = \mathcal{S}_{24}(\omega) = \mathcal{S}_{31}(\omega) = \mathcal{S}_{34}(\omega) = \mathcal{S}_{42}(\omega) = \mathcal{S}_{43}(\omega) = 0 \tag{G.11}$$

For the conventional Willis media, the local Willis couplings ($k = 0$) vanish when the system preserve the parity symmetry (Liu et al., 2019; Pernas-Salomón and Shmuel, 2020a,b; Li et al., 2022, 2024; Qu et al., 2022). However, the local Willis couplings $\mathcal{S}_{14}(\omega)$, $\mathcal{S}_{23}(\omega)$, $\mathcal{S}_{32}(\omega)$, and $\mathcal{S}_{41}(\omega)$ of our metabeam still exist when the system has the parity symmetry. Additionally, when our metabeam preserves parity symmetry, the off-diagonal local elastic and density constants are zero, while the diagonal local elastic and density constants remain nonzero.

Symmetry analysis of the microscopic medium

Through the sensor-actuator system, the parity symmetry of the local constitutive relation can be broken. Here we show how this microscopic symmetry breaking leads to broken parity symmetry in the macroscopic constitutive coefficients. For the local constitutive matrix, if the system preserves parity symmetry, its entries must satisfy

$$\beta_{12}(\omega) = \beta_{13}(\omega) = \beta_{21}(\omega) = \beta_{24}(\omega) = \beta_{31}(\omega) = \beta_{34}(\omega) = \beta_{42}(\omega) = \beta_{43}(\omega) = 0. \tag{G.12}$$

These constraints enforce that all couplings between fields of opposite parity vanish. In the homogenized description, nonzero Willis couplings or asymmetric compliance require violating at least one of these conditions; thus, once any of the above equalities is broken, the parity symmetry of the macroscopic medium is also broken. In our active metabeam, the sensor-actuator feedback creates nonzero β_{21} breaks this microscopic parity symmetry, which in turn leads to broken parity symmetry in the macroscopic constitutive tensor and enables nonzero Willis couplings.

Appendix H. Causality and Kramers-Kronig relations

Here we appeal to the principle of causality and Kramers-Kronig relations, according to which the response at time t is determined only by the field at the present and at earlier times $t' \leq t$.

The constitutive relation in reciprocal space depends on both frequency and wavenumber, indicating nonlocality in both spatial and temporal domains. In the space-time domain, causality and a finite signal speed c imply that the response kernel vanishes outside the causal cone,

$$\boldsymbol{\mathcal{S}}(x,t) = 0 \quad \text{for } t < 0 \text{ or } |x| > ct, \tag{H.1}$$

so that only sources inside the cone $|x| \leq ct$ and $t' \leq t$ contribute to the response at (x,t). In the space-time domain, the nonlocal constitutive relation for a spatially and temporally homogeneous medium can be written as (Leontovich, 1961; Sun and Puri, 1989; Shokri and Rukhadze, 2019)

$$\boldsymbol{\mathcal{E}}(x,t) = \int_0^t \mathrm{d}t' \int_{-ct'}^{ct'} \mathrm{d}x'\, \boldsymbol{\mathcal{S}}(x-x', t-t')\, \boldsymbol{\Sigma}(x',t'), \tag{H.2}$$

where c denotes the maximum group velocity of the medium. For the Timoshenko beam in our nondimensionalization, the group velocity approaches $c = 1$ as $k \to \infty$, so we may take $c = 1$ as the maximal signal speed. The time integral is restricted to $t' \in [0, t]$ by causality, and the spatial integral to $|x' - x| \leq c(t - t')$, ensuring that the response at position x and time t depends only on sources that lie within the causal cone and have had sufficient time for their influence to propagate to x. Considering plane-wave propagation, the space-time convolution can be written in the (k,ω) domain as

$$\boldsymbol{\mathcal{E}}(k,\omega) = \boldsymbol{\mathcal{S}}(k,\omega)\, \boldsymbol{\Sigma}(k,\omega), \tag{H.3}$$

where we define the space-time Fourier transform of the response kernel as

$$\boldsymbol{\mathcal{S}}(\omega,k) = \int_0^\infty \mathrm{d}t \int_{-ct}^{ct} \mathrm{d}x\, \boldsymbol{\mathcal{S}}(x,t)\, e^{i(\omega t + kx)}, \tag{H.4}$$

using the causal support $t > 0$ and $|x| \leq ct$. Conversely, the kernel in the space-time domain is obtained from

$$\boldsymbol{\mathcal{S}}(x,t) = \frac{1}{4\pi^2} \int_{-\infty}^{\infty}\int_{-\infty}^{\infty} \boldsymbol{\mathcal{S}}(\omega,k)\, e^{-i(\omega t + kx)}\, \mathrm{d}\omega\, \mathrm{d}k \tag{H.5}$$

.

Therefore, using the inverse space-time Fourier representation of $\boldsymbol{\mathcal{S}}(x,t)$, we obtain

$$\begin{aligned}
\boldsymbol{\mathcal{S}}(\omega,k) &= \int_0^\infty \mathrm{d}t\, e^{i\omega t} \int_{-ct}^{ct} \mathrm{d}x\, e^{ikx}\, \boldsymbol{\mathcal{S}}(x,t) \\
&= \frac{1}{4\pi^2} \int_0^\infty \mathrm{d}t\, e^{i\omega t} \int_{-ct}^{ct} \mathrm{d}x \int_{-\infty}^{\infty}\int_{-\infty}^{\infty} \boldsymbol{\mathcal{S}}(\omega',k') e^{-i\omega' t - ik'x + ikx} \mathrm{d}\omega' \mathrm{d}k' \\
&= \frac{1}{4\pi^2} \int_{-\infty}^{\infty}\int_{-\infty}^{\infty} \boldsymbol{\mathcal{S}}(\omega',k') \mathrm{d}\omega' \mathrm{d}k' \int_0^\infty \mathrm{d}t\, e^{i(\omega-\omega')t} \int_{-ct}^{ct} \mathrm{d}x\, e^{i(k-k')x} \\
&= \frac{1}{4\pi^2} \int_{-\infty}^{\infty}\int_{-\infty}^{\infty} \boldsymbol{\mathcal{S}}(\omega',k') \mathrm{d}\omega' \mathrm{d}k' \int_0^\infty \frac{1}{i(k-k')} \left[e^{i(\omega-\omega'+ck-ck')t} - e^{i(\omega-\omega'-ck'-ck)t} \right] \mathrm{d}t.
\end{aligned} \tag{H.6}$$

To ensure convergence of the time integral, we add a small positive imaginary part $i\delta$ ($\delta > 0$) to the frequency,

$$\begin{aligned}\boldsymbol{\mathcal{S}}(\omega,k) &= \frac{1}{4\pi^2}\int_{-\infty}^{\infty}\int_{-\infty}^{\infty}\frac{\boldsymbol{\mathcal{S}}(\omega',k')}{i(k-k')}\left[\frac{-1}{i(\omega-\omega'+c(k-k')+i\delta)}+\frac{1}{i(\omega-\omega'+c(k'-k)+i\delta)}\right]\mathrm{d}\omega'\mathrm{d}k' \\ &= -\frac{1}{2\pi^2}\int_{-\infty}^{\infty}\int_{-\infty}^{\infty}\frac{\boldsymbol{\mathcal{S}}(\omega',k')}{(\omega-\omega'+c(k'-k)+i\delta)(\omega-\omega'+c(k-k')+i\delta)}\mathrm{d}\omega'\mathrm{d}k'.\end{aligned} \tag{H.7}$$

Following the procedure of Sun and Puri (Sun and Puri, 1989), and using the fact that $\boldsymbol{\mathcal{S}}(\omega,k)$ is analytic in the upper half of the ω-plane for fixed k (causality), the above double integral can be recast in the one-dimensional "dispersion" form

$$\boldsymbol{\mathcal{S}}(\omega,k) = \frac{1}{2\pi i}\int_{-\infty}^{\infty}\frac{\boldsymbol{\mathcal{S}}\big(\omega',\,k+(\omega'-\omega)/c\big)}{\omega'-\omega-i\delta}\,\mathrm{d}\omega'. \tag{H.8}$$

Applying the Plemelj formula then yields the wavenumber-dependent Kramers-Kronig relations

$$\begin{aligned}\mathrm{Re}\left[\boldsymbol{\mathcal{S}}(\omega,k)\right] &= \frac{1}{\pi}\mathcal{P}\int_{-\infty}^{\infty}\frac{\mathrm{Im}\left[\boldsymbol{\mathcal{S}}\big(\omega',\,k+(\omega'-\omega)/c\big)\right]}{\omega'-\omega}\,\mathrm{d}\omega', \\ \mathrm{Im}\left[\boldsymbol{\mathcal{S}}(\omega,k)\right] &= -\frac{1}{\pi}\mathcal{P}\int_{-\infty}^{\infty}\frac{\mathrm{Re}\left[\boldsymbol{\mathcal{S}}\big(\omega',\,k+(\omega'-\omega)/c\big)\right]}{\omega'-\omega}\,\mathrm{d}\omega'.\end{aligned} \tag{H.9}$$

In the limiting case of an infinite signal velocity, $c \to \infty$, the k-shift inside the integrand becomes negligible and the relations reduce to the standard frequency-only Kramers-Kronig formulas

$$\begin{aligned}\mathrm{Re}\left[\boldsymbol{\mathcal{S}}(\omega,k)\right] &= \frac{1}{\pi}\mathcal{P}\int_{-\infty}^{\infty}\frac{\mathrm{Im}\left[\boldsymbol{\mathcal{S}}(\omega',k)\right]}{\omega'-\omega}\,\mathrm{d}\omega', \\ \mathrm{Im}\left[\boldsymbol{\mathcal{S}}(\omega,k)\right] &= -\frac{1}{\pi}\mathcal{P}\int_{-\infty}^{\infty}\frac{\mathrm{Re}\left[\boldsymbol{\mathcal{S}}(\omega',k)\right]}{\omega'-\omega}\,\mathrm{d}\omega'.\end{aligned} \tag{H.10}$$

References

Agranovich, V.M., Ginzburg, V., 2013. Crystal Optics With Spatial Dispersion, and Excitons. Vol. 42. Springer Science & Business Media.
Altman, C., Suchy, K., 2011. Reciprocity, Spatial Mapping and Time Reversal in Electromagnetics. Springer Science & Business Media.
Alù, A., 2011. First-principles homogenization theory for periodic metamaterials. Phys. Rev. B-Condensed Matter Mater. Phys. 84 (7), 075153.
Ashida, Y., Gong, Z., Ueda, M., 2020. Non-hermitian physics. Adv. Phys. 69 (3), 249–435.
Baz, A., 2024. Why active willis metamaterials? a controllability and observability perspective. J. Acoust. Soc. Am. 156 (5), 3338–3352.
Chen, J., Chen, Y., Xu, X., Zhou, W., Huang, G., 2022. A physics-guided machine learning for multifunctional wave control in active metabeams. Extreme Mech. Lett. 55, 101827.
Chen, Y., Haberman, M.R., 2023. Controlling displacement fields in polar willis solids via gauge transformations. Phys. Rev. Lett. 130 (14), 147201.
Chen, Y., Li, X., Hu, G., Haberman, M.R., Huang, G., 2020. An active mechanical willis meta-layer with asymmetric polarizabilities. Nat. Commun. 11 (1), 3681.
Chen, Y., Li, X., Scheibner, C., Vitelli, V., Huang, G., 2021. Realization of active metamaterials with odd micropolar elasticity. Nat. Commun. 12 (1), 5935.
Cheng, W., Hu, G., 2022. Acoustic skin effect with non-reciprocal willis materials. Appl. Phys. Lett. 121 (4).
Jackson, J.D., 2012. Classical Electrodynamics. Wiley. https://books.google.com/books?id=8qHCZjJHRUgC.
Lee, J.-H., Zhang, Z., Gu, G.X., 2023. Dynamic homogenization of heterogeneous piezoelectric media: a polarization approach using infinite-body green's function. J. Mech. Phys. Solids 181, 105442.
Leontovich, M., 1961. Generalization of the kramers-kronig formulas to media with spatial dispersion. Sov. Phys. JETP-USSR 13 (3), 634–637.
Leung, K.M., Qiu, Y., 1993. Multiple-scattering calculation of the two-dimensional photonic band structure. Phys. Rev. B 48 (11), 7767.
Li, Z., Han, P., Hu, G., 2024. Willis dynamic homogenization method for acoustic metamaterials based on multiple scattering theory. J. Mech. Phys. Solids 189, 105692.
Li, Z., Qu, H., Zhang, H., Liu, X., Hu, G., 2022. Interfacial wave between acoustic media with willis coupling. Wave Motion 112, 102922.
Liu, Y., Liang, Z., Zhu, J., Xia, L., Mondain-Monval, O., Brunet, T., Alù, A., Li, J., 2019. Willis metamaterial on a structured beam. Phys. Rev. X 9 (1), 011040.
Liu, Z., Chan, C.T., Sheng, P., Goertzen, A.L., Page, J.H., 2000. Elastic wave scattering by periodic structures of spherical objects: theory and experiment. Phys. Rev. B 62 (4), 2446.
Martin, P.A., 2006. Multiple Scattering: Interaction of Time-harmonic Waves With N Obstacles. 107, Cambridge University Press.
Milton, G.W., 2007. New metamaterials with macroscopic behavior outside that of continuum elastodynamics. New J. Phys. 9 (10), 359.
Milton, G.W., Briane, M., Willis, J.R., 2006. On cloaking for elasticity and physical equations with a transformation invariant form. New J. Phys. 8 (10), 248.
Milton, G.W., Willis, J.R., 2010. Minimum variational principles for time-harmonic waves in a dissipative medium and associated variational principles of hashin–shtrikman type. Proc. Royal Soc. A Engineering Sciences 466 (2122), 3013–3032.
Muhafra, K., Haberman, M.R., Shmuel, G., 2023. Discrete one-dimensional models for the electromomentum coupling. Phys. Rev. Appl. 20 (1), 014042.
Muhlestein, M.B., Sieck, C.F., Wilson, P.S., Haberman, M.R., 2017. Experimental evidence of willis coupling in a one-dimensional effective material element. Nat. Commun. 8 (1), 15625.
Nassar, H., He, Q.-C., Auffray, N., 2015. Willis elastodynamic homogenization theory revisited for periodic media. J. Mech. Phys. Solids 77, 158–178.
Nassar, H., He, Q.-C., Auffray, N., 2016. On asymptotic elastodynamic homogenization approaches for periodic media. J. Mech. Phys. Solids 88, 274–290.
Nassar, H., Yousefzadeh, B., Fleury, R., Ruzzene, M., Alù, A., Daraio, C., Norris, A.N., Huang, G., Haberman, M.R., 2020. Nonreciprocity in acoustic and elastic materials. Nat. Rev. Mater. 5 (9), 667–685.
Nemat-Nasser, S., Srivastava, A., 2011. Overall dynamic constitutive relations of layered elastic composites. J. Mech. Phys. Solids 59 (10), 1953–1965.
Norris, A.N., Shuvalov, A.L., Kutsenko, A.A., 2012. Analytical formulation of three-dimensional dynamic homogenization for periodic elastic systems. Proc. Royal Soc. A Engineering Sciences 468 (2142), 1629–1651.
Okuma, N., Kawabata, K., Shiozaki, K., Sato, M., 2020. Topological origin of non-hermitian skin effects. Phys. Rev. Lett. 124 (8), 086801.
Pernas-Salomón, R., Haberman, M.R., Norris, A.N., Shmuel, G., 2021. The electromomentum effect in piezoelectric willis scatterers. Wave Motion 106, 102797.
Pernas-Salomón, R., Shmuel, G., 2018. Dynamic homogenization of composite and locally resonant flexural systems. J. Mech. Phys. Solids 119, 43–59.
Pernas-Salomón, R., Shmuel, G., 2020a. Fundamental principles for generalized willis metamaterials. Phys. Rev. Appl. 14 (6), 064005.
Pernas-Salomón, R., Shmuel, G., 2020b. Symmetry breaking creates electro-momentum coupling in piezoelectric metamaterials. J. Mech. Phys. Solids 134, 103770.
Ponge, M.-F., Poncelet, O., Torrent, D., 2017. Dynamic homogenization theory for nonlocal acoustic metamaterials. Extreme Mech. Lett. 12, 71–76.
Qian, H., Chen, J., Wang, S., Shao, N., Liu, K., Huang, G., 2025. Non-hermitian elastic metabeams with nonlinear and nonlocal coupling: physical realization and topological wave manipulation. Adv. Funct. Mater. , e18194.

Qu, H., Liu, X., Hu, G., 2022. Mass-spring model of elastic media with customizable willis coupling. Int. J. Mech. Sci. 224, 107325.
Rabczuk, T., Ren, H., Zhuang, X., 2023. Computational methods based on peridynamics and nonlocal operators. In: Computational Methods in Engineering & the Sciences. Springer.
Shokri, B., Rukhadze, A.A., 2019. Electrodynamics of Conducting Dispersive Media. Springer.
Shore, R.A., Yaghjian, A.D., 2007. Traveling waves on two-and three-dimensional periodic arrays of lossless scatterers. Radio Sci. 42 (06), 1–40.
Shuvalov, A.L., Kutsenko, A.A., Norris, A.N., Poncelet, O., 2011. Effective willis constitutive equations for periodically stratified anisotropic elastic media. Proc. Royal Soc. A Engineering Sciences 467 (2130), 1749–1769.
Sieck, C.F., Alù, A., Haberman, M.R., 2017. Origins of willis coupling and acoustic bianisotropy in acoustic metamaterials through source-driven homogenization. Phys. Rev. B 96 (10), 104303.
Srivastava, A., 2015. Elastic metamaterials and dynamic homogenization: a review. Int. J. Smart Nano Materials 6 (1), 41–60.
Sun, J.G., Puri, A., 1989. Kramers-kronig relations in media with spatial dispersion. Opt. Commun. 70 (1), 33–37.
Wang, S., Hu, Z., Wu, Q., Chen, H., Prodan, E., Zhu, R., Huang, G., 2023. Smart patterning for topological pumping of elastic surface waves. Sci. Adv. 9 (30), eadh4310.
Wang, S., Shao, N., Chen, H., Chen, J., Qian, H., Wu, Q., Duan, H., Alu, A., Huang, G., 2025. Temporal refraction and reflection in modulated mechanical metabeams: theory and physical observation. arXiv Preprint arXiv:2501.09989.
Wang, X., Zhang, X.-G., Yu, Q., Harmon, B.N., 1993. Multiple-scattering theory for electromagnetic waves. Phys. Rev. B 47 (8), 4161.
Wang, Y., Wu, Q., Tian, Y., Huang, G., 2024. Non-hermitian wave dynamics of odd plates: microstructure design and theoretical modelling. J. Mech. Phys. Solids 182, 105462.
Willis, J.R., 1981. Variational principles for dynamic problems for inhomogeneous elastic media. Wave Motion 3 (1), 1–11.
Willis, J.R., 1997. Dynamics of composites. In: Continuum Micromechanics. Springer, pp. 265–290.
Willis, J.R., 2009. Exact effective relations for dynamics of a laminated body. Mech. Mater. 41 (4), 385–393.
Willis, J.R., 2011. Effective constitutive relations for waves in composites and metamaterials. Proc. Royal Soc. A Engineering Sciences 467 (2131), 1865–1879.
Willis, J.R., 2012. The construction of effective relations for waves in a composite. Comptes rendus. Mécanique 340 (4–5), 181–192.
Wu, Q., Wang, S., Qian, H., Wang, Y., Huang, G., 2024. Understanding of topological mode and skin mode morphing in 1d and 2d non-hermitian resonance-based meta-lattices. J. Mech. Phys. Solids 193, 105907.
Wu, Q., Xu, X., Qian, H., Wang, S., Zhu, R., Yan, Z., Ma, H., Chen, Y., Huang, G., 2023. Active metamaterials for realizing odd mass density. Proc. Nation. Acad. Sci. 120 (21), e2209829120.
Xia, Y., Riva, E., Rosa, M. I.N., Cazzulani, G., Erturk, A., Braghin, F., Ruzzene, M., 2021. Experimental observation of temporal pumping in electromechanical waveguides. Phys. Rev. Lett. 126 (9), 095501.
Yao, S., Wang, Z., 2018. Edge states and topological invariants of non-hermitian systems. Phys. Rev. Lett. 121 (8), 086803.
Yao, W., Zhong, W., Lim, C.W., 2009. Symplectic Elasticity. World Scientific.
Yokomizo, K., Murakami, S., 2019. Non-bloch band theory of non-hermitian systems. Phys. Rev. Lett. 123 (6), 066404.
Zhai, Y., Kwon, H.-S., Popa, B.-I., 2019. Active willis metamaterials for ultracompact nonreciprocal linear acoustic devices. Phys. Rev. B 99 (22), 220301.
Zhang, K., Yang, Z., Fang, C., 2020. Correspondence between winding numbers and skin modes in non-hermitian systems. Phys. Rev. Lett. 125 (12), 126402.